Super-Resolution in Time-Reversal Acoustics

Peter Blomgren* George Papanicolaou† Hongkai Zhao‡

August 25, 2001

Abstract

We analyze theoretically and with numerical simulations the phenomenon of super-resolution in time-reversal acoustics. A signal that is recorded and then re-transmitted by an array of transducers, propagates back though the medium and refocuses approximately on the source that emitted it. In a homogeneous medium, the refocusing resolution of the time-reversed signal is limited by diffraction. When the medium has random inhomogeneities the resolution of the refocused signal can in some circumstances beat the diffraction limit. This is super-resolution.

We give a theoretical treatment of this phenomenon and present numerical simulations which confirm the theory.

1 Introduction

In time-reversal acoustics a signal is recorded by an array of transducers, time-reversed and then re-transmitted into the medium. The re-transmitted signal propagates back through the same medium and refocuses approximately on the source. The refocusing is approximate because of the finite size of the array of transducers (receivers and transmitters), which is called a *Time Reversal Mirror* (TRM; see figure 1). The possibility of refocusing by time-reversal has many important applications in medicine, geophysics, non-destructive testing, underwater acoustics, wireless communications, etc., and has been studied in a variety of settings [Fin97, Fin99, HSK+99, DJ90]. In the frequency domain, time-reversal is equivalent to phase-conjugation which has been studied extensively in optics [Por89].

Time-reversed signals propagate backwards through the time-independent medium and go through all the multiple scattering, reflections and refraction that they underwent in the forward direction, which is why refocusing occurs. However, the size of the TRM is often small compared to the propagation distance, that is, the aperture of the time-reversal mirror is small, and only a

*Dept. of Math., Stanford University, Stanford, CA 94305; blomgren@math.Stanford.EDU.
Work supported by grants AFOSR F49620-98-1-0211 and NSF-DMS-9971972.
†Dept. of Math., Stanford University, Stanford, CA 94305; papanico@math.Stanford.EDU.
Work supported by grants AFOSR F49620-98-1-0211 and NSF-DMS-9971972.
‡Dept. of Math., University of California, Irvine, CA 92697-3875; zhao@math.uci.edu.

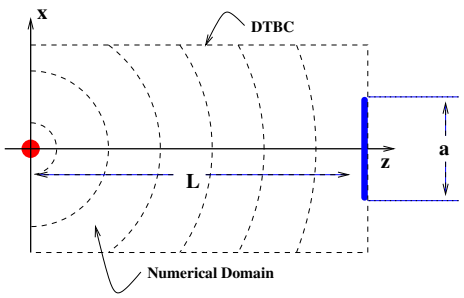

Figure 1: Setting for time-reversal acoustics. A point source (red) emits a wave, which is received on a screen (blue) of width a — the *time-reversal mirror (TRM)* — at a distance L from the source. The domain of numerical solution of the (parabolic) wave equation is shown with a dotted line, and DTBC stands for *Discrete Transparent Boundary Conditions.*

small part of the advancing wave is captured and time reversed. In homogeneous media, the spatial resolution of the time-reversed signals is limited by diffraction and is inversely proportional to the aperture size and proportional to the wavelength times the propagation distance. In the notation of figure 1, the time-reversed and back-propagated signal due to a point source will focus in a region around the source with spatial width of order $\lambda L/a$. Here λ is the wavelength of the carrier signal for the pulse, L is the distance from the source to the TRM and a is the size of the TRM.

In underwater acoustics, typical parameters are: propagation speed $c_0 = 1.5$km/s, wavelength $\lambda = 1$m, propagation distance $L = 1 \sim 50$km, TRM size $a = 50 \sim 100$m. In non-destructive testing with ultrasound these lengths are scaled by a factor 10^{-3}, so that typical wavelengths are $\lambda = 1$mm.

If the medium is randomly inhomogeneous the focusing resolution of the back-propagated signal can be better than the resolution in the homogeneous case. This is referred to as *super-resolution*. Roughly speaking, the random inhomogeneities produce multipathing and the TRM appears to have an aperture that is larger than its physical size, an *effective aperture* $a_e > a$. This means that the re-compressed pulse is narrower than in the homogeneous medium and we have super-resolution with a spatial scale of order $\lambda L/a_e$. This phenomenon was observed in underwater acoustics experiments [DJ90, HSK$^+$99, KHS$^+$97] as well as in the ultra-sound regime [DRF95, Fin97, Fin99].

An attempt at a theoretical explanation of super-resolution by multipathing is given in [DJ92]. This, however, requires *ensemble averages* in random media and does not account for the remarkable stability of the compressed pulse, without any averaging, as seen in the actual experiments. In figure 2, numerical computations with time-harmonic signals illustrate the lack of any resolution realization-by-realization, while on average the resolution is remarkable. For time-harmonic signals, time reversal is the same as phase conjugation on the

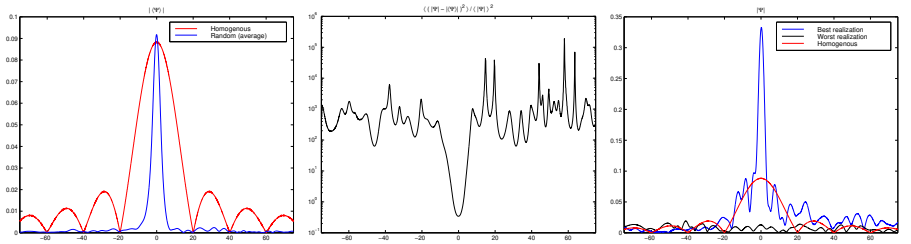

(a) Average (b) Relative Variance (c) Realizations

Figure 2: Time-harmonic waves in random media. Propagation distance `1000m`, TRM width `50m`, width of numerical domain `150m`, width of random medium `112.5m`, contrast ±`5%`, `428` realizations. (a) Amplitude of the mean: Homogeneous (red) and average over random realizations (blue) case. (b) Relative variance, $> \mathcal{O}(1)$ except for a very small interval. (c) Individual realizations that show super-resolution (blue) as well as no resolution at all (black).

TRM (usually called the *Phase Conjugation Mirror*, in this setting).

The key to the statistical stability of time-reversed signals is their frequency spread. This stabilization of pulses has been seen in other contexts in stochastic equations and random media [SP00] but not in connection with time-reversal, as it is presented and analyzed here.

In this paper, we explore analytically and numerically the phenomenon of super-resolution in time reversal in a regime of parameters where the effects of the random medium are fully developed. This regime can be described roughly as follows. The propagation distance, L, the carrier wavelength, λ, the aperture of the TRM, a, the correlation length of the medium fluctuations, l, and the variance of the sound speed fluctuations, $\left\langle \mu^2 \right\rangle$, are scaled by a single parameter $\epsilon = \lambda/L$, which we assume to be small. We assume also that $l \sim \lambda$ and that $\left\langle \mu^2 \right\rangle \sim \epsilon$. In this regime:

- The propagation distance is much larger than the correlation length of the inhomogeneities, which is large or comparable to the wavelength.
- The aperture of the TRM is relatively small so that the effect of the random medium and multipathing can be felt.
- The random fluctuations of the propagation speed are weak so that waves are scattered mostly in the forward direction.

Many situations in underwater acoustics and in ultrasound propagation fall in this regime.

The objectives of this paper are to:

- Systematically calculate statistics of the the back-propagated phase-conjugated field using transport and Wigner equations in the frequency domain.

- Derive an *effective aperture* formula for a TRM in random media. In particular, we show that the effective aperture for a finite aperture or Gaussian TRM is
$$a_e(L) = a\sqrt{1 + \frac{L^3\gamma}{a^2}},$$
where γ is a constant with dimensions of reciprocal length that depends on the statistics of the fluctuations of the propagation speed (see section 7 for details). It is assumed that the effective aperture is still small compared to the propagation distance, $a_e(L) \ll L$.

- Show that for a pulse in the time domain, super-resolution is linked to the *effective aperture*, a_e, of the TRM, and that self-averaging due to the frequency spread of the signal makes super-resolution in time-reversal statistically stable.

In section 2, we set up equations for back-propagated fields and quantities of interest in the frequency domain. In section 3, we introduce an invariant embedding approach in order to derive transport and Winger equations for the time-reversed signal originating from a point source. Then, in section 4, the diffraction limit for a homogeneous medium is calculated, in both the frequency and time domain for Gaussian and finite aperture TRMs. Scaling for the Wigner equation for the transport limit, from which the effective aperture will be derived, is introduced in section 5. Pulse stabilization in the time domain and the beam approximation are discussed in sections 6 and 7, respectively. Details of the numerical implementation and numerical results are shown in section 8. The concept of dynamic TRM placement is introduced in section 9 and is explored with numerical simulations. Finally in section 10 we consider time-reversal in a waveguide and show the results of several numerical simulations without discussing here the theory that explains them. In Appendix A we explain carefully the various scaling limits which lead to super-resolution and statistical stability in the time domain as described here.

2 Back-Propagated Fields

The time-reversed signal is synthesized from time-harmonic waves by the inverse Fourier transform. We start with the Helmholtz equation for time-harmonic waves $u(x, y, z)e^{-i\omega t}$

$$(1) \quad u_{xx} + u_{yy} + u_{zz} + k^2 n^2(x, y, z)u = 0.$$

Here $k = \frac{\omega}{c_0}$ is the wavenumber, c_0 is a reference speed, $c(x, y, z)$ is the propagation speed and $n(x, y, z) = \frac{c_0}{c(x,y,x)}$ is the index of refraction. When the time reversal mirror has small aperture (beam geometry) and the fluctuations in the propagation speed are weak, we can use the parabolic or paraxial approximation (see [Tap77]). We let $u = e^{ikz}\psi(x, y, z)$ and ignore backscattering in the Helmholtz equation (the term ψ_{zz}) to obtain a parabolic initial value problem

for the wave amplitude ψ, in which the direction of propagation z plays the role of time (see [BEHJ88])

$$(2)\qquad \begin{cases} 2ik\psi_z + \Delta_\perp \psi + k^2\left(n^2-1\right)\psi = 0, & \Delta_\perp \text{ is the transverse Laplacian} \\ \psi|_{z=0} = \psi_0(\mathbf{x};k), & \mathbf{x} = (x,y). \end{cases}$$

We note that the parabolic approximation is not valid in the immediate neighborhood of a point source. The full Helmholtz equation must be solved near the source and then matched with the parabolic equation further away from it. We will use a Gaussian beam in the frequency domain as an initial wave amplitude ψ_0, that is, a Gaussian in the transverse space coordinates. We take the pulse to be Gaussian in time as well, which means a Gaussian in the wavenumber k or frequency ω. By Fourier synthesis the wave function in the time domain is given by

$$(3)\qquad \Psi(t,x,y,z) = \int e^{i\omega(z/c_0-t)}\psi(x,y,z;\omega/c_0)\,d\omega.$$

We will also use a point source and consider it as the limit of a Gaussian in space whose width is very small or zero.

The Green's function $G(z,z_0;\mathbf{x},\xi;k)$ with a point source at (z_0,ξ) satisfies

$$(4)\qquad \begin{cases} 2ikG_z + \Delta_{\mathbf{x}} G + k^2\mu(\mathbf{x},z)G = 0, \quad z > z_0, \quad \mu(\mathbf{x},z) = n^2(\mathbf{x},z) - 1 \\ G(z_0,z_0;\mathbf{x},\xi;k) = \delta(\mathbf{x}-\xi). \end{cases}$$

By reciprocity $G(z,z_0;\mathbf{x},\xi;k) = G(z_0,z;\xi,\mathbf{x};k)$. If the initial source distribution at $z_0 = 0$ is $\psi_0(\eta;k)$ then the wave field at $z = L$ is

$$(5)\qquad \psi(\mathbf{y},L;k) = \int G(L,0;\mathbf{y},\eta;k)\psi_0(\eta;k)\,d\eta.$$

In time-reversal problems it is convenient to introduce the tensor product of two Green's functions

$$(6)\qquad \begin{cases} \Gamma(L,\mathbf{x},\mathbf{y};\xi,\eta;k) &=& G(L,0;\mathbf{x},\xi;k)\,\overline{G(L,0;\mathbf{y},\eta;k)} \\ \Gamma(0,\mathbf{x},\mathbf{y};\xi,\eta;k) &=& \delta(\mathbf{x}-\xi)\,\delta(\mathbf{y}-\eta) \end{cases}$$

because $\Gamma(L,\mathbf{y},\mathbf{y};\xi,\eta;k)$ describes the response, at the source plane, of a point source at η, whose signal is recorded on the TRM at $\mathbf{y}$, phase-conjugated, back-propagated and observed at ξ. In the following section we derive an equation for Γ, which is a form of invariant embedding.

Using $\Gamma(L,\mathbf{y},\mathbf{y};\xi,\eta;k)$, the time-harmonic, phase-conjugated and back-propagated field at the source plane, $z = 0$, can be written as

$$(7)\qquad \begin{aligned} \psi^B(\xi,L;k) &= \int G(L,0;\mathbf{y},\xi;k)\overline{\psi(\mathbf{y},L;k)}\chi_A(\mathbf{y})\,d\mathbf{y} \\ &= \iint \chi_A(\mathbf{y})\overline{\psi_0(\eta;k)}G(L,0;\mathbf{y},\xi;k)\overline{G(L,0;\mathbf{y},\eta;k)}\,d\eta\,d\mathbf{y} \\ &= \iint \chi_A(\mathbf{y})\overline{\psi_0(\eta;k)}\Gamma(L,\mathbf{y},\mathbf{y};\xi,\eta;k)\,d\eta\,d\mathbf{y}. \end{aligned}$$

Here $\chi_A(\mathbf{y})$ is the aperture function for the TRM occupying the region A and is equal to 1 if $\mathbf{y} \in A$, and 0 otherwise. We use the same notation for other aperture functions as well. The back-propagated time-reversed field is obtained by Fourier synthesis

$$\Psi^B(\xi, L, t) = \int \psi^B(\xi, L; \omega/c_0) e^{-it\omega}\, d\omega. \tag{8}$$

Here t is *relative* time, on the scale of the pulse width. The travel-time to and from the TRM has been eliminated.

3 Invariant Embedding and the Wigner Equation

From the equation for the Green's function $G(z, z_0; \mathbf{x}, \xi; k)$ we can derive an equation for $\Gamma(L, \mathbf{x}, \mathbf{y}; \xi, \eta; k)$

$$\begin{cases} 2ik\dfrac{\partial \Gamma}{\partial L} + (\Delta_{\mathbf{x}} - \Delta_{\mathbf{y}})\,\Gamma + k^2\left(\mu(\mathbf{x}, L) - \mu(\mathbf{y}, L)\right)\Gamma = 0 \\ \Gamma(0, \mathbf{x}, \mathbf{y}; \xi, \eta; k) = \delta(\mathbf{x} - \xi)\,\delta(\mathbf{y} - \eta). \end{cases} \tag{9}$$

Here $\Delta_{\mathbf{x}}$ and $\Delta_{\mathbf{y}}$ are the Laplacians in the transverse variable $\mathbf{x}$ and $\mathbf{y}$, respectively. We introduce the following change of transverse variables

$$\begin{cases} \mathbf{X} = \dfrac{\mathbf{x}+\mathbf{y}}{2}, \quad \mathbf{x} = \mathbf{X} - \dfrac{\mathbf{Y}}{2} \\ \mathbf{Y} = \mathbf{y} - \mathbf{x}, \quad \mathbf{y} = \mathbf{X} + \dfrac{\mathbf{Y}}{2} \\ \Delta_{\mathbf{x}} - \Delta_{\mathbf{y}} = (\nabla_{\mathbf{x}} - \nabla_{\mathbf{y}})(\nabla_{\mathbf{x}} + \nabla_{\mathbf{y}}) = -2\nabla_{\mathbf{X}}\nabla_{\mathbf{Y}}. \end{cases} \tag{10}$$

This transforms equation (9) into

$$\begin{cases} 2ik\dfrac{\partial \Gamma}{\partial L} - 2\nabla_{\mathbf{X}}\nabla_{\mathbf{Y}}\Gamma + k^2\left(\mu\left(\mathbf{X} - \frac{\mathbf{Y}}{2}, L\right) - \mu\left(\mathbf{X} + \frac{\mathbf{Y}}{2}, L\right)\right)\Gamma = 0 \\ \Gamma(0, \mathbf{X}, \mathbf{Y}; \xi, \eta; k) \stackrel{\text{def}}{=} \delta\left(\mathbf{X} - \frac{\mathbf{Y}}{2} - \xi\right)\,\delta\left(\mathbf{X} + \frac{\mathbf{Y}}{2} - \eta\right). \end{cases} \tag{11}$$

With the Fourier transform defined by

$$\begin{cases} \widehat{f}(p) = \dfrac{1}{(2\pi)^d}\displaystyle\int_{R^d} e^{ip\cdot x} f(x)\, dx \\ f(x) = \displaystyle\int_{R^d} e^{-ip\cdot x}\widehat{f}(p)\, dp \end{cases} \tag{12}$$

and the scaling rule $\delta(x) = |\alpha|^d \delta(\alpha x)$ for δ functions in d dimensions, with $d = 1, 2$ here, we introduce the Wigner distribution

$$W(L, \mathbf{X}, \mathbf{P}; \xi, \eta; k) = \frac{1}{(2\pi)^d}\int e^{i\mathbf{P}\cdot\mathbf{Y}}\Gamma(L, \mathbf{X}, \mathbf{Y}; \xi, \eta; k)\, d\mathbf{Y}. \tag{13}$$

It satisfies the Wigner equation (Fourier transform in $\mathbf{Y}$ of the Γ-equation)

$$
\begin{aligned}
&k\frac{\partial W}{\partial L} + \mathbf{P}\cdot\nabla_{\mathbf{X}} W = \\
&\quad \tfrac{ik^2}{2}\int e^{-i\mathbf{Q}\cdot\mathbf{X}}\widehat{\mu}(\mathbf{Q},L)\Big[W\left(L,\mathbf{X},\mathbf{P}+\tfrac{\mathbf{Q}}{2}\right) - W\left(L,\mathbf{X},\mathbf{P}-\tfrac{\mathbf{Q}}{2}\right)\Big]\,d\mathbf{Q},
\end{aligned}
\tag{14}
$$

with initial condition

$$
W(0,\mathbf{X},\mathbf{P};\xi,\eta;k) = \frac{1}{(2\pi)^d}\, e^{-i\mathbf{P}\cdot(\xi-\eta)}\delta\left(\mathbf{X}-\tfrac{\xi+\eta}{2}\right). \tag{15}
$$

Here $\widehat{\mu}(\mathbf{P},L)$ is the Fourier transform of $\mu(\mathbf{x},L)$ in the transverse variable $\mathbf{x}$. We can recover Γ from W by a Fourier transform, and in particular

$$
\Gamma(L,\mathbf{y},\mathbf{y};\xi,\eta;k) = \int W(L,\mathbf{y},\mathbf{P};\xi,\eta)\,d\mathbf{P}. \tag{16}
$$

Thus, the phase-conjugated back-propagated time harmonic field is given by

$$
\psi^B(\xi,L;k) = \iint \overline{\psi_0(\eta;k)}\chi_A(\mathbf{y})\left(\int W(L,\mathbf{y},\mathbf{P};\xi,\eta;k)\,d\mathbf{P}\right)d\mathbf{y}\,d\eta, \tag{17}
$$

in terms of the solution W of the Wigner equation (14).

4 Deterministic Diffraction Limit

In this section we will use the expression (17) for the back-propagated field and the invariant embedding and Wigner equations from section 3 to calculate the deterministic diffraction limit for a time-dependent pulse, emanating from a point source in space.

For a homogeneous medium, with $\mu \equiv 0$, the solution to the Wigner equation (14) with initial condition (15) is

$$
W(L,\mathbf{X},\mathbf{P};\xi,\eta) = \frac{1}{(2\pi)^d}\, e^{-i\mathbf{P}\cdot(\xi-\eta)}\delta\left(\mathbf{X}-\tfrac{L\mathbf{P}}{k}-\tfrac{\xi+\eta}{2}\right). \tag{18}
$$

Now, equation (16) gives

$$
\begin{aligned}
\Gamma(L,\mathbf{y},\mathbf{y};\xi,\eta;k) &= \int W(L,\mathbf{y},\mathbf{P};\xi,\eta)\,d\mathbf{P} \\
&= \tfrac{1}{(2\pi)^d}\left(\tfrac{k}{L}\right)^d e^{-i\frac{k}{L}\left(\mathbf{y}-\frac{\xi+\eta}{2}\right)\cdot(\xi-\eta)}.
\end{aligned}
\tag{19}
$$

From this we get the following expression for the phase-conjugated and back-propagated time harmonic field:

$$
\begin{aligned}
\psi^B(\xi,L;k) &= \iint \overline{\psi_0(\eta,k)}\chi_A(\mathbf{y})\tfrac{1}{(2\pi)^d}\left(\tfrac{k}{L}\right)^d e^{-i\frac{k}{L}\left(\mathbf{y}-\frac{\xi+\eta}{2}\right)\cdot(\xi-\eta)}\,d\mathbf{y}\,d\eta \\
&= \left(\tfrac{k}{L}\right)^d \int \widehat{\chi}_A\left(\tfrac{k}{L}(\eta-\xi)\right)\overline{\psi_0(\eta,k)}e^{i\frac{k(\xi^2-\eta^2)}{2L}}\,d\eta \\
&= \left(\tfrac{k}{L}\right)^d e^{i\frac{k\xi^2}{2L}}\int \widehat{\chi}_A\left(\tfrac{k}{L}(\eta-\xi)\right)e^{-i\frac{k\eta^2}{2L}}\overline{\psi_0(\eta,k)}\,d\eta.
\end{aligned}
\tag{20}
$$

Here $\widehat{\chi}_A$ is the Fourier transform of the aperture function χ_A. If the source is a δ-function in space (point source), $\psi_0(\eta) = \delta(\eta)$, then the expression for ψ^B simplifies to

$$\psi^B(\xi, L; k) = \left(\frac{k}{L}\right)^d e^{i\frac{k\xi^2}{2L}}\, \widehat{\chi}_A\left(\frac{-k\xi}{L}\right). \tag{21}$$

We will now use this result for two different types of time reversal mirrors. First, we consider a finite aperture TRM, from which we have edge diffraction effects. Then, we consider a TRM with a Gaussian aperture function. We comment briefly on the resolution limits in time-reversal for these two kinds of TRMs.

4.1 Finite Aperture TRM

For simplicity we consider only one transverse dimension, $d = 1$. Let $\chi_A(y)$ be the indicator function of a TRM of size a centered at $y = 0$. The Fourier transform of $\chi_A(y)$ is $\widehat{\chi}_A(P) = \frac{\sin Pa/2}{\pi P}$. Plugging this into equation (21) gives

$$\psi^B(\xi, L; k) = \frac{1}{\pi\xi}\, \sin\left(\frac{k\xi a}{2L}\right) e^{i\frac{k\xi^2}{2L}}. \tag{22}$$

The diffraction limited resolution can be measured by the distance ξ_F from the origin to the first *Fresnel Zone*, that is, the first zero of the phase-conjugated back-propagated field

$$\xi_F = \frac{2\pi L}{ka} = \frac{\lambda L}{a}. \tag{23}$$

If the pulse is a point source in space and a Gaussian in the time domain with carrier frequency ω_0, that is,

$$\Psi_0(\eta, t) = \delta(\eta)\frac{1}{\sqrt{2\pi\sigma_t^2}} e^{-\frac{t^2}{2\sigma_t^2}} e^{-i\omega_0 t},\ \psi_0(\eta, \omega) = \frac{1}{2\pi}\delta(\eta) e^{-\frac{(\omega-\omega_0)^2\sigma_t^2}{2}}, \tag{24}$$

then the *time-reversed* and back-propagated signal in time at the source plane is

$$\begin{aligned}
\Psi^B(\xi, L, t) = &\ \tfrac{1}{2\pi}\textstyle\int \psi^B(\xi, L, \frac{\omega}{c_0}) e^{-\frac{(\omega-\omega_0)^2\sigma_t^2}{2}} e^{-i\omega t}\, d\omega \\
= &\ \textstyle\int \frac{1}{(2\pi)^2 i\xi}\left(e^{\frac{i\omega\xi a}{2c_0L}} - e^{-\frac{i\omega\xi a}{2c_0L}}\right) e^{\frac{i\omega\xi^2}{2c_0L}} e^{-\frac{(\omega-\omega_0)^2\sigma_t^2}{2}} e^{-i\omega t}\, d\omega \\
= &\ \frac{1}{(2\pi)^{3/2} i\xi\sigma_t} e^{-i\omega_0\left(t-\frac{\xi^2}{2c_0L}\right)} \left\{ e^{\frac{i\omega_0\xi a}{2c_0L}} e^{-\frac{\left[(t-\frac{\xi^2}{2c_0L})-\frac{\xi a}{2c_0L}\right]^2}{2\sigma_t^2}} \right. \\
&\ \left. - e^{\frac{-i\omega_0\xi a}{2c_0L}} e^{-\frac{\left[(t-\frac{\xi^2}{2c_0L})+\frac{\xi a}{2c_0L}\right]^2}{2\sigma_t^2}} \right\}.
\end{aligned} \tag{25}$$

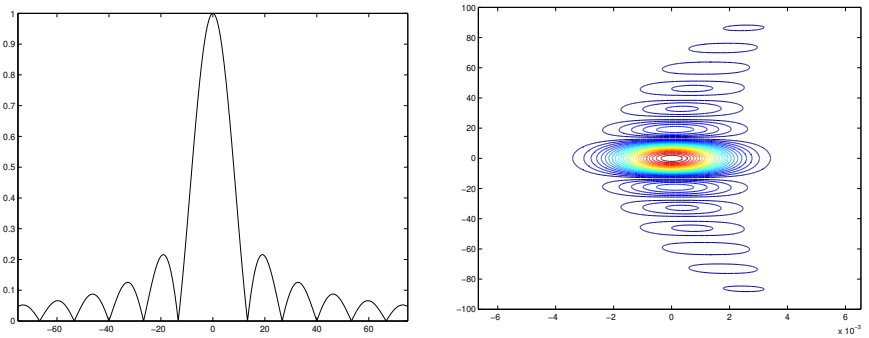

Figure 3: The left figure shows the spatial diffraction pattern of the amplitude of (25) at time $t = 0$. The right figure is a space-time contour plot of the amplitude of (25) and shows the parabolic shift in arrival time. Here the pulse width is $\sigma_t = 1.33$ms, the TRM width $a = 50$m, the propagation speed is $c_0 = 1500$m/s, the propagation distance is $L = 1000$m, and the period of the carrier is 0.22ms at 4.5KHz.

Diffraction from the two edges of the TRM is seen clearly. At the wave front, where $t = \frac{\xi^2}{2c_0 L}$, we have

$$\Psi^B(\xi, L, \frac{\xi^2}{2c_0 L}) = \frac{\sqrt{2\pi}}{\sigma_t} \frac{1}{2\pi^2 \xi} \sin\left[\frac{\omega_0 \xi a}{2c_0 L}\right] e^{-\xi^2/2\left[\frac{2\sigma_t c_0 L}{a}\right]^2}. \quad (26)$$

If the width of the pulse in time σ_t is large compared to λ_0/c_0, the time period, then the variance of the Gaussian in Ψ^B is

$$\frac{2\sigma_t c_0 L}{a} = \frac{2\sigma_t c_0}{\lambda_0} \frac{\lambda_0 L}{a} \gg \xi_F = \frac{\lambda_0 L}{a}. \quad (27)$$

Thus, the diffraction limit is determined by the carrier frequency. A plot of $\Psi^B(\xi, L, 0)$ is shown in figure 3.

4.2 Gaussian TRM

We now consider the case where the aperture function, χ_A, is a normalized, isotropic Gaussian with variance a,

$$\chi_A(\mathbf{y}) \sim \frac{1}{(2\pi a^2)^{\frac{d}{2}}} e^{-\frac{|\mathbf{y}|^2}{2a^2}}. \quad (28)$$

In this case, the phase-conjugated back-propagated time-harmonic field from a point source is

$$\psi^B(\xi, L; k) = \left(\frac{k}{2\pi L}\right)^d e^{-\frac{a^2 k^2 |\xi|^2}{2L^2}} e^{i\frac{k|\xi|^2}{2L}}. \quad (29)$$

The resolution of the refocused signal is proportional to the variance of this Gaussian, which is $\frac{\lambda L}{a}$.

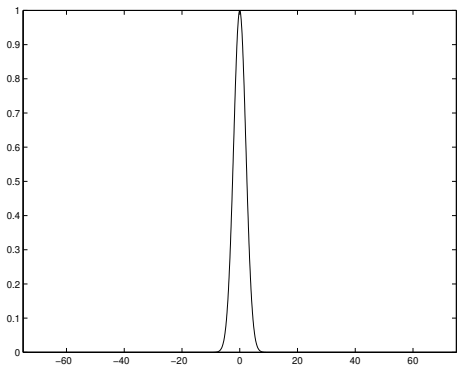

Figure 4: The spatial shape of the compressed pulse with a Gaussian aperture function at time $t = 0$, from (31). Here the pulse width is $\sigma_t = 1.33$ms, the TRM width is $a = 50$m, the propagation speed is $c = 1500$m/s, propagation distance is $L = 1000$m, and the time period of the carrier is 0.22ms. Note the absence of Fresnel zones for a Gaussian TRM.

If the pulse is a point source in space and a real Gaussian in time with carrier frequency ω_0 then

$$\Psi_0(\eta,t)=\delta(\eta)\frac{1}{\sqrt{2\pi\sigma_t^2}}e^{-\frac{t^2}{2\sigma_t^2}}e^{-i\omega_0 t},\ \psi_0(\eta,\omega)=\frac{\delta(\eta)}{2\pi}e^{-\frac{(\omega-\omega_0)^2\sigma_t^2}{2}}. \tag{30}$$

We use the inverse Fourier transform to synthesize the self-averaging, time-reversed and back-propagated signal at the source plane

$$\begin{aligned}\Psi^B(\xi,L,t)&=\tfrac{1}{2\pi}\int\psi^B(\xi,L,\tfrac{\omega}{c_0})e^{-\frac{(\omega-\omega_0)^2\sigma_t^2}{2}}e^{-i\omega t}\,d\omega\\&=\tfrac{1}{2\pi}\int\left(\frac{\omega}{2\pi c_0 L}\right)^d e^{-\frac{a^2\omega^2\xi^2}{2c_0^2L^2}}e^{\frac{i\omega\xi^2}{2c_0L}}e^{-\frac{(\omega-\omega_0)^2\sigma_t^2}{2}}e^{-i\omega t}\,d\omega=\frac{1}{2\pi}\left(\frac{i}{2\pi c_0 L}\right)^d\cdot\\&\frac{d^d}{dt^d}\left[e^{-i\omega_0\left(t-\frac{\xi^2}{2c_0L}\right)}e^{-\frac{a^2\omega_0^2\xi^2}{2c_0^2L^2}}\sqrt{\frac{2\pi}{\frac{a^2\xi^2}{c_0^2L^2}+\sigma_t^2}}e^{\frac{\left[i\left(t-\frac{\xi^2}{2c_0L}\right)+\frac{a^2\omega_0\xi^2}{c_0^2L^2}\right]^2}{\frac{2a^2\xi^2}{c_0^2L^2}+2\sigma_t^2}}\right].\end{aligned} \tag{31}$$

Here $\frac{\xi^2}{2c_0L}$ is the a parabolic shift in time of the front and $d = 1, 2$. A plot of the absolute value of this function at $t = 0$ is shown in figure 4. When the aperture is small, $\frac{a}{L} \ll 1$, and the time duration of the pulse is large compared to the time period of the carrier, $\sigma_t \gg \frac{\lambda_0}{c_0}$ then the width of the compressed pulse in space is approximately $\lambda_0 L/a$. With the parameters as in figure 4 this ratio is 6.6m, which is roughly the width at mid level of the curve shown.

5 Scaled Wigner Equation and the Transport Limit

In order to study the effect of random inhomogeneities we introduce a scaling of parameters as follows: *(i)* The wavelength λ is short compared to the propagation distance L and we let $\epsilon = \frac{\lambda}{L} \ll 1$ be a small dimensionless parameter which scales all other variables. *(ii)* The wavelength is comparable to the correlation length, l, that is $l \sim \lambda$. This allows full interaction between the waves and the random medium, which is the interesting case to study. *(iii)* The fluctuations, $\mu = n^2 - 1$, of the index of refraction are weak and isotropic, $|\mu| \sim \sqrt{\epsilon}$. If the fluctuations are very strong or very anisotropic (as in a layered medium) the parabolic wave equation cannot be used. If they are very weak then stochastic effects will not be observable.

We want to analyze long distance and long time propagation so we rescale the space variables by $\mathbf{x} \to \frac{\mathbf{x}}{\epsilon}$, $L \to \frac{L}{\epsilon}$. We do not rescale the time $t \to \frac{t}{\epsilon}$ in (8) because in this paper t is always *relative* time on the scale of the pulse width. So it will remain of order one. The Green's function in the scaled variables is

$$(32)\quad \begin{cases} G^\epsilon(L,0;\mathbf{x},\xi;k) &= G(\frac{L}{\epsilon},0;\frac{\mathbf{x}}{\epsilon},\frac{\xi}{\epsilon};k), \\ \Gamma^\epsilon(L,\mathbf{x},\mathbf{y};\xi,\eta;k) &= G^\epsilon(L,0;\mathbf{x},\xi;k)\overline{G}^\epsilon(L,0;\mathbf{y},\eta;k), \end{cases}$$

and Γ^ϵ satisfies the scaled equation

$$(33)\quad \begin{cases} 2ik\epsilon\dfrac{\partial\Gamma^\epsilon}{\partial L} + \epsilon^2\left(\Delta_{\mathbf{x}} - \Delta_{\mathbf{y}}\right)\Gamma^\epsilon + k^2\sqrt{\epsilon}\left[\mu(\dfrac{\mathbf{x}}{\epsilon},\dfrac{L}{\epsilon}) - \mu(\dfrac{\mathbf{y}}{\epsilon},\dfrac{L}{\epsilon})\right]\Gamma^\epsilon = 0 \\ \Gamma^\epsilon(0,\mathbf{x},\mathbf{y};\xi,\eta;k) = \dfrac{1}{\epsilon}\delta\left(\dfrac{\mathbf{x}-\xi}{\epsilon}\right)\delta\left(\dfrac{\mathbf{y}-\eta}{\epsilon}\right). \end{cases}$$

The scaling of the initial conditions for Γ^ϵ is adjusted so that the wave energy is independent of the small parameter ϵ.

Since we are interested in the local coherence of wave fields, within a few wavelengths or correlation lengths, we introduce the scaled change of variables

$$(34)\quad \begin{cases} \mathbf{X} &= \dfrac{\mathbf{x}+\mathbf{y}}{2}, \quad \mathbf{x} &= \mathbf{X} - \dfrac{\epsilon\mathbf{Y}}{2} \\ \epsilon\mathbf{Y} &= \mathbf{y}-\mathbf{x}, \quad \mathbf{y} &= \mathbf{X} + \dfrac{\epsilon\mathbf{Y}}{2}, \end{cases}$$

so that $\Delta_{\mathbf{x}} - \Delta_{\mathbf{y}} = \left(\nabla_{\mathbf{x}} - \nabla_{\mathbf{y}}\right)\left(\nabla_{\mathbf{x}} + \nabla_{\mathbf{y}}\right) = -\frac{2}{\epsilon}\nabla_{\mathbf{X}}\nabla_{\mathbf{Y}}$. In the new variables $\Gamma^\epsilon(L,\mathbf{X},\mathbf{Y};\xi,\eta;k)$ satisfies

$$(35)\quad \begin{cases} 2ik\dfrac{\partial\Gamma^\epsilon}{\partial L} - 2\nabla_{\mathbf{X}}\nabla_{\mathbf{Y}}\Gamma^\epsilon + \dfrac{k^2}{\sqrt{\epsilon}}\left(\mu\left(\frac{\mathbf{X}}{\epsilon} - \frac{\mathbf{Y}}{2},\frac{L}{\epsilon}\right) - \mu\left(\frac{\mathbf{X}}{\epsilon} + \frac{\mathbf{Y}}{2},\frac{L}{\epsilon}\right)\right)\Gamma^\epsilon = 0 \\ \Gamma^\epsilon(0,\mathbf{X},\mathbf{Y};\xi,\eta;k) = \dfrac{1}{\epsilon}\delta\left(\frac{\mathbf{X}}{\epsilon} - \frac{\mathbf{Y}}{2} - \frac{\xi}{\epsilon}\right)\delta\left(\frac{\mathbf{X}}{\epsilon} + \frac{\mathbf{Y}}{2} - \frac{\eta}{\epsilon}\right). \end{cases}$$

We again let $W^\epsilon(L,\mathbf{X},\mathbf{P};\xi,\eta;k)$ be the Fourier transform of $\Gamma^\epsilon(L,\mathbf{X},\mathbf{Y};\xi,\eta;k)$ in $\mathbf{Y}$ and then W^ϵ satisfies

$$\begin{aligned} &k\frac{\partial W^\epsilon}{\partial L}+\mathbf{P}\cdot\nabla_{\mathbf{X}}W^\epsilon = \\ &\tfrac{ik^2}{2\sqrt{\epsilon}}\int e^{-\frac{i\mathbf{Q}\cdot\mathbf{X}}{\epsilon}}\widehat{\mu}(\mathbf{Q},\tfrac{L}{\epsilon})\Big[W^\epsilon\left(L,\mathbf{X},\mathbf{P}+\tfrac{\mathbf{Q}}{2}\right)-W^\epsilon\left(L,\mathbf{X},\mathbf{P}-\tfrac{\mathbf{Q}}{2}\right)\Big]\,d\mathbf{Q}, \end{aligned} \tag{36}$$

with initial condition

$$W^\epsilon(0,\mathbf{X},\mathbf{P};\xi,\eta;k)=\frac{1}{(2\pi)^d}\,e^{-i\mathbf{P}\cdot\frac{(\xi-\eta)}{\epsilon}}\delta(\mathbf{X}-\tfrac{\xi+\eta}{2}). \tag{37}$$

By the asymptotic theory that we review briefly in Appendix A, the average Wigner function $\langle\, W^\epsilon(L,\mathbf{X},\mathbf{P};\xi,\eta;k)\,\rangle \to W(L,\mathbf{X},\mathbf{P};\xi,\eta;k)$, as $\epsilon\to 0$, and W satisfies the transport equation

$$\begin{cases} k\frac{\partial W}{\partial L}+\mathbf{P}\cdot\nabla_{\mathbf{X}}W=\frac{\pi k^3}{4}\cdot \\ \quad\int\widehat{R}\left(\frac{\mathbf{P}^2-\mathbf{Q}^2}{2k},\mathbf{P}-\mathbf{Q}\right)\Big[W(L,\mathbf{X},\mathbf{Q};\xi,\eta;k)-W(L,\mathbf{X},\mathbf{P};\xi,\eta;k)\Big]\,d\mathbf{Q} \\ W(0,\mathbf{X},\mathbf{P};\xi,\eta;k)=\frac{e^{-i\mathbf{P}\cdot(\xi-\eta)/\epsilon}}{(2\pi)^d}\delta\left(\mathbf{X}-\frac{\xi+\eta}{2}\right), \end{cases} \tag{38}$$

where R is the correlation function

$$R(z,\mathbf{x})=\langle\,\mu(\eta,\mathbf{y})\mu(\eta+z,\mathbf{y}+\mathbf{x})\,\rangle\,, \tag{39}$$

and $\widehat{R}(p,\mathbf{P})$ is its Fourier transform in $(z,\mathbf{x})$, that is, the power spectral density of the fluctuations of the refractive index.

It is important to note that the initial condition for W in (38) depends on the small parameter ϵ, even though we have passed to the asymptotic limit in the equation. Small ϵ means high frequency asymptotics, that is, long propagation distances compared to the wavelength, as well as long propagation distances compared to the correlation length, which produces the incoherent scattering terms on the right side of the equation in (38). By keeping the ϵ dependence of the initial conditions we retain coherent diffraction effects in the transport approximation, which are clearly important in time reversal.

In Appendix A we discuss several scaling limits in which multipathing effects are relevant. We also discuss the validity of the paraxial approximation in these limits. In particular, the paraxial approximation may be violated in the transport limit but its validity is restored in the narrow beam limit of section 7.

6 Pulse Stabilization

As we noted in the introduction, time reversal of time harmonic or very narrow band signals (phase conjugation) is statistically unstable. This means that

$$\langle\,\psi^B(\xi,L,k)\,\rangle=\iint\left[\int W(L,\mathbf{y},\mathbf{P};\xi,\eta;k))\,d\mathbf{P}\right]\overline{\psi_0(\eta,k)}\chi_A(\mathbf{y})\,d\mathbf{y}\,d\eta \tag{40}$$

gives no information at all about the behavior of $\psi^B(\xi, L, k)$ for individual realizations of the medium, as demonstrated in figure 2 which is obtained by numerical simulations. How is it then that super-resolution in time reversal is seen clearly in a variety of physical experiments where there is no ensemble of random media or averaging? This issue is not addressed in the time reversal literature and poor understanding of it tends to make super-resolution counter-intuitive and somewhat mysterious, especially to those familiar with phase conjugation.

The explanation is that super-resolution is a time domain phenomenon and it is the re-compressed pulse in space *and* time that is statistically stable. Pulse stabilization in randomly layered media is well understood, [SP00] and references therein, and the reason for this stabilization is similar to the one encountered in time reversal here. In the asymptotic limit of high frequency, short correlations and long propagation distances, described in the previous section, we also have statistical decorrelation of the wave functions for different frequencies. For $k \neq k'$ we have

$$\left\langle \psi^B(L,\xi,k)\psi^B(L,\xi,k') \right\rangle \approx \left\langle \psi^B(L,\xi,k) \right\rangle \left\langle \psi^B(L,\xi,k') \right\rangle, \tag{41}$$

in the limit $\epsilon \to 0$. This is the property that gives pulse stabilization in the time domain. To see this, we note that the time-reversed, back-propagated field is

$$\Psi^B(L,\xi,t) = \int e^{-i\omega t}\psi^B(L,\xi,\omega/c_0)\, d\omega, \tag{42}$$

and thus

$$\begin{aligned}
\left\langle \Psi^B(L,\xi,t)^2 \right\rangle &= \left\langle \left(\int e^{-i\omega t}\psi^B(L,\xi,\frac{\omega}{c_0})\, d\omega \right)^2 \right\rangle \\
&= \int\int e^{-i(\omega_1+\omega_2)t} \left\langle \psi^B(L,\xi,\frac{\omega_1}{c_0})\psi^B(L,\xi,\frac{\omega_2}{c_0}) \right\rangle d\omega_1 d\omega_2 \\
&\approx \int\int e^{-i(\omega_1+\omega_2)t} \left\langle \psi^B(L,\xi,\frac{\omega_1}{c_0}) \right\rangle \left\langle \psi^B(L,\xi,\frac{\omega_2}{c_0}) \right\rangle d\omega_1 d\omega_2 \\
&= \left\langle \Psi^B(L,\xi,t) \right\rangle^2 .
\end{aligned} \tag{43}$$

This means that for any $\delta > 0$, the probability

$$\begin{aligned}
&P\{|\Psi^B(L,\xi,t) - \left\langle \Psi^B(L,\xi,t) \right\rangle| > \delta\} \\
&\qquad \leq \frac{\left\langle \left(\Psi^B(L,\xi,t) - \left\langle \Psi^B(L,\xi,t) \right\rangle\right)^2 \right\rangle}{\delta^2} \approx 0,
\end{aligned} \tag{44}$$

by the Chebyshev inequality and (43). That is,

$$\Psi^B(L,\xi,t) \approx \left\langle \Psi^B(L,\xi,t) \right\rangle, \tag{45}$$

so that the time-reversed and back-propagated field is *self-averaging in this asymptotic regime*. Put in another way, averaging over frequencies is like averaging over realizations, *in the appropriate asymptotic regime*, as discussed in

Appendix A. This is why super-resolution is observed in physical situations as well as in numerical simulations. In section 8 we will discuss figures 7, 8, and 9 where the self-averaging property is quite clearly seen in the numerical simulations.

From (43) it is clear that, in general, fluctuation statistics of the time-reversed and back-propagated field depend on the two-frequency correlation function $\left\langle \psi^B(L,\xi,\omega_1/c_0)\psi^B(L,\xi,\omega_2/c_0)\right\rangle$. This differs substantially from its incoherent limit $\left\langle \psi^B(L,\xi,\omega_1/c_0)\right\rangle\left\langle \psi^B(L,\xi,\omega_2/c_0)\right\rangle$ only when $|\omega_1-\omega_2| \approx \epsilon\,(\omega_1+\omega_2)/2$. The two-frequency correlation function can be expressed in terms of the two-frequency Wigner function for which a transport equation like (38) can be derived for its evolution in L. The additional information obtained this way affects only the tail of the time-reversed and back-propagated field, a phenomenon that is well understood in randomly layered media [SP00, AKP$^+$91]. Tail behavior, that is, large t behavior of (8), and hence two-frequency statistics, is important in a more refined theory of super-resolution where there are several sources of different strengths, in different but nearby locations in space as well as in time. We then want to get theoretical limits of when these sources can be discriminated in the time-reversed and back-propagated field and for that we do need to know the tail behavior.

7 Beam Geometry

We will assume from now on that the difference $\xi-\eta$ is of order ϵ and we will drop the ϵ in the phase of the initial condition in the transport equation (38). This means that we will restrict our attention to the behavior of the time-reversed, back-propagated field in the vicinity of the source.

We will now introduce the *beam approximation* for the the solution W of the transport equation (38). This is simply a diffusion approximation in $\mathbf{P}$ space that is valid when the power spectral density $\widehat{R}(p,\mathbf{P})$ is peaked near zero in the transverse wavenumber $\mathbf{P}$. We will describe this approximation qualitatively without introducing a small parameter and doing a formal asymptotic analysis. We do this because it is a relatively simple and well known approximation, and in any case does not involve high-frequency asymptotics or statistical considerations like the derivation of (38). The narrow beam approximation is discussed further in Appendix A.

The physical basis for the narrow beam approximation is this: When we are in the transport regime and the aperture of the TRM is small, that is, $a \ll L$ in figure 1, then only multiply scattered waves that stay near the z axis contribute significantly to the time-reversed and back-propagated field. So the wave goes over many correlation lengths in the direction of propagation but only over a few in the transverse direction. This is what makes the power spectral density appear to be peaked in the transverse direction.

A quick derivation of the beam approximation is as follows. We expand W

around the point $\mathbf{P}$ up to second order on the right side of (38) to obtain

$$(46)\quad \begin{cases} k\dfrac{\partial W}{\partial L} + \mathbf{P}\cdot\nabla_{\mathbf{X}} W = \dfrac{\pi k^3}{4}\displaystyle\int \widehat{R}\left(\tfrac{\mathbf{P}^2-\mathbf{Q}^2}{2k}, \mathbf{P}-\mathbf{Q}\right)\cdot \\ \qquad \left[\nabla W(\mathbf{P}) + \tfrac{1}{2}\nabla\nabla W(\mathbf{P})(\mathbf{Q}-\mathbf{P})\right]\cdot(\mathbf{Q}-\mathbf{P})\, d\mathbf{Q} \\ W(0,\mathbf{X},\mathbf{P};\xi,\eta;k) = \dfrac{1}{(2\pi)^d} e^{-i\mathbf{P}\cdot(\xi-\eta)}\delta\left(\mathbf{X} - \tfrac{\xi+\eta}{2}\right), \end{cases}$$

where $\nabla\nabla W$ is the matrix of second derivatives of W. The gradient term on the right is zero because $\widehat{R}$ is even, so (46) becomes

$$(47)\quad \begin{cases} k\dfrac{\partial W}{\partial L} + \mathbf{P}\cdot\nabla_{\mathbf{X}} W = \dfrac{\pi k^3 D(\mathbf{P})}{8}\Delta_{\mathbf{P}} W(\mathbf{P}) \\ W(0,\mathbf{X},\mathbf{P};\xi,\eta;k) = \dfrac{1}{(2\pi)^d} e^{-i\mathbf{P}\cdot(\xi-\eta)}\delta\left(\mathbf{X} - \tfrac{\xi+\eta}{2}\right), \end{cases}$$

where $\Delta_{\mathbf{P}}$ is the Laplacian in wavenumber space and the wavenumber diffusion constant $D(\mathbf{P})$ is given by

$$(48)\quad D(\mathbf{P}) \stackrel{\text{def}}{=} \int \widehat{R}\left(\tfrac{\mathbf{P}^2-\mathbf{Q}^2}{2k}, \mathbf{P}-\mathbf{Q}\right)|\mathbf{P}-\mathbf{Q}|^2\, d\mathbf{Q}.$$

When this wavenumber diffusion constant, which is a reciprocal length, is essentially independent of the wavenumber $\mathbf{P}$ then equation (47) is the narrow beam approximation to the transport equation (38). In many interesting scaling limits the phase space diffusion coefficient D does turn out to be constant, as we discuss in Appendix A.

For D constant, equation (47) can be solved by elementary methods. To get the time-reversed, back-propagated field we need $\Gamma(L,\mathbf{y},\mathbf{y};\xi,\eta;k)$, which is the inverse Fourier transform of W at $\mathbf{Y}=0$. Thus,

$$(49)\quad \begin{aligned} \Gamma(L,\mathbf{y},\mathbf{y};\xi,\eta;k) &= \textstyle\int W(L,\mathbf{y},\mathbf{P};\xi,\eta;k)\, d\mathbf{P} \\ &= \left[\tfrac{k}{2\pi L}\right]^d e^{-i\frac{k}{L}\left(\mathbf{y}-\frac{\xi+\eta}{2}\right)\cdot(\xi-\eta)}\, e^{-\pi k^2 D L(\xi-\eta)^2/2}. \end{aligned}$$

Let

$$(50)\quad \gamma = \frac{\pi D}{8}.$$

Then the mean phase-conjugated and back-propagated time-harmonic field is given by

$$(51)\quad \begin{aligned} \left\langle\, \psi^B(\xi,L,k)\,\right\rangle &= \iint \left[\textstyle\int W(L,\mathbf{y},\mathbf{P};\xi,\eta;k))\, d\mathbf{P}\right] \overline{\psi_0(\eta,k)}\chi_A(\mathbf{y})\, d\mathbf{y}\, d\eta \\ &= \left(\tfrac{k}{L}\right)^d e^{i\frac{k\xi^2}{2L}} \textstyle\int \widehat{\chi}_A\left(\frac{k}{L}(\eta-\xi)\right) e^{-i\frac{k\eta^2}{2L}}\overline{\psi_0(\eta,k)} e^{-\gamma L k^2(\xi-\eta)^2}\, d\eta. \end{aligned}$$

Comparing this result with the exact solution of the deterministic phase-conjugated and back-propagated field (20), we see that the effect of the random

medium is just the Gaussian factor $e^{-\gamma L k^2 (\xi-\eta)^2}$. Using (51) we can now compute an *effective aperture* for the phase-conjugated (or time-reversed) and back-propagated mean field due to a point source in the case of Gaussian TRM and finite aperture TRM, in both the frequency and the time domain.

7.1 Gaussian TRM

For a point source and a Gaussian aperture of the form (28) we obtain from (51)

$$\left\langle \psi^B(\xi, L; k) \right\rangle = \left(\frac{k}{2\pi L}\right)^d e^{-\left(\frac{a^2}{2L^2}+\gamma L\right)k^2\xi^2} e^{i\frac{k\xi^2}{2L}}. \tag{52}$$

Comparing this with the deterministic field (29) we determine an *effective aperture* for the TRM for the mean time-harmonic wave,

$$a_e = a\sqrt{1+\frac{2\gamma L^3}{a^2}}. \tag{53}$$

This result was also derived in a different way in [DJ92]. We will see that it is essentially universally valid in the beam approximation, both in the frequency and in the time domain. It is clearly not valid unless

$$\frac{a_e(L)}{L} \ll 1, \tag{54}$$

which means that the *effective* TRM aperture size must be consistent with the beam approximation. From (53) and from the numerical experiments that we report in section 8 it is clear that $a_e(L) \gg a$ when the propagation distance L is large.

The self-averaging, time-reversed and back-propagated field can be calculated exactly as in the deterministic case by replacing a with a_e in equation (31). If $a_e = a_e(L)$ is much smaller than the propagation distance L, as it must be by (54), then our analysis for the deterministic field carries over, which means that we get the same a_e in the time domain.

Super-resolution is now precisely the phenomenon of having the self-averaging, time-reversed and back-propagated field be essentially equal to the deterministic field with a replaced by a_e, which is much larger than a for L large. The width in space of the re-compressed field is proportional to $\lambda_0 L/a_e$ where λ_0 is the wavelength of the carrier wave.

7.2 Finite Aperture TRM

With a finite aperture TRM the formula for the compressed pulse is more complicated. Stochastic, multipathing effects modify edge diffraction from the TRM, in the time domain, in a complicated way. The mean phase-conjugated and back-propagated time harmonic field is

$$\left\langle \psi^B(\xi, L; k) \right\rangle = \frac{1}{\pi\xi} \sin\left(\frac{k\xi a}{2L}\right) e^{i\frac{k\xi^2}{2L}} e^{-\gamma L k^2 \xi^2}. \tag{55}$$

We do a Fourier synthesis to get the self-averaged, time-reversed and back-propagated signal in the time domain for a point source, Gaussian pulse. The result is a combination of (25) and (31),

$$
\begin{aligned}
\Psi^B(\xi,L,t) = & \int \psi^B(\xi,L,\tfrac{\omega}{c_0}) e^{-\frac{(\omega-\omega_0)^2\sigma_t^2}{2}} e^{-i\omega t}\, d\omega \\
= & \int \frac{1}{2\pi i\xi}\left[e^{\frac{i\omega\xi a}{2c_0L}} - e^{-\frac{i\omega\xi a}{2c_0L}}\right] e^{\frac{i\omega\xi^2}{2c_0L}} e^{-\frac{\gamma^2 L\omega^2\xi^2}{c_0^2}} e^{\frac{(\omega-\omega_0)^2\sigma_t^2}{2}} e^{-i\omega t}\, d\omega \\
= & \frac{1}{2\pi i\xi}\sqrt{\frac{\pi}{\frac{\sigma_t^2}{2}+\frac{\gamma^2 L\xi^2}{c_0^2}}}\, e^{-i\omega_0\left(t-\frac{\xi^2}{2c_0L}\right)} e^{-\frac{\gamma^2 L\omega_0^2\xi^2}{c_0^2}} \\
& \left\{ e^{\frac{i\omega_0\xi a}{2c_0L}} e^{\frac{\left[i(t-\frac{\xi^2}{2c_0L})-i\frac{\xi a}{2c_0L}+\frac{2\gamma^2 L\omega_0\xi^2}{c_0^2}\right]^2}{2\sigma_t^2+\frac{4\gamma^2L\xi^2}{c_0^2}}} \right. \\
& \left. -e^{\frac{-i\omega_0\xi a}{2c_0L}} e^{\frac{\left[i(t-\frac{\xi^2}{2c_0L})+i\frac{\xi a}{2c_0L}+\frac{2\gamma^2 L\omega_0\xi^2}{c_0^2}\right]^2}{2\sigma_t^2+\frac{4\gamma^2L\xi^2}{c_0^2}}} \right\}.
\end{aligned}
\tag{56}
$$

In figure 5 we show formula (56) at $t=0$, with various parameter values. We use the effective aperture formula

$$
a_e = a\sqrt{1+\frac{2\gamma L^3}{\left(\frac{a}{2}\right)^2}},
\tag{57}
$$

which is like the Gaussian TRM effective aperture formula (53) but with the constants adjusted using the numerical results presented in section 8. In all calculations we use the estimate $\gamma = 2.12\times 10^{-5} m^{-1}$ that we obtained from direct numerical simulations. This is discussed further in the next section.

The effective aperture formula (57), or (53), cannot be used when L is too small, so that there is not enough multipathing, or too large so that the beam approximation is not valid. We must have $a_e(L) \ll L$. Using (57), this means that $L \ll (8\gamma)^{-1} \approx 6km$. The range $300-400m$ to $1km$ is roughly where the effective aperture formula is valid for random media like the one we simulated. At $600m$ the effective TRM aperture is already $195m$, nearly five times larger than the physical size of the TRM, which is $40m$.

At the wave front, $t=\frac{\xi^2}{2c_0L}$, expression (56) becomes

$$
\begin{aligned}
\Psi^B(\xi,L,t=\tfrac{\xi^2}{2c_0L}) = & \frac{1}{2\pi i\xi}\sqrt{\frac{\pi}{\frac{\sigma_t^2}{2}+\frac{\gamma^2 L\xi^2}{c_0^2}}}\, e^{-\frac{\left(\frac{a^2}{4c_0^2L^2}+\frac{2\sigma_t^2\gamma^2L\omega_0^2}{c_0^2}\right)\xi^2}{2\sigma_t^2+\frac{4\gamma^2L\xi^2}{c_0^2}}} \cdot \\
& \left\{ e^{\frac{i\omega_0\xi a}{2c_0L}} e^{-\frac{i2a\gamma^2\omega_0^2\xi^3}{2c_0^3\sigma_t^2+4c_0\gamma^2L\xi^2}} - e^{-\frac{i\omega_0\xi a}{2c_0L}} e^{\frac{i2a\gamma^2\omega_0^2\xi^3}{2c_0^3\sigma_t^2+4c_0\gamma^2L\xi^2}} \right\}.
\end{aligned}
\tag{58}
$$

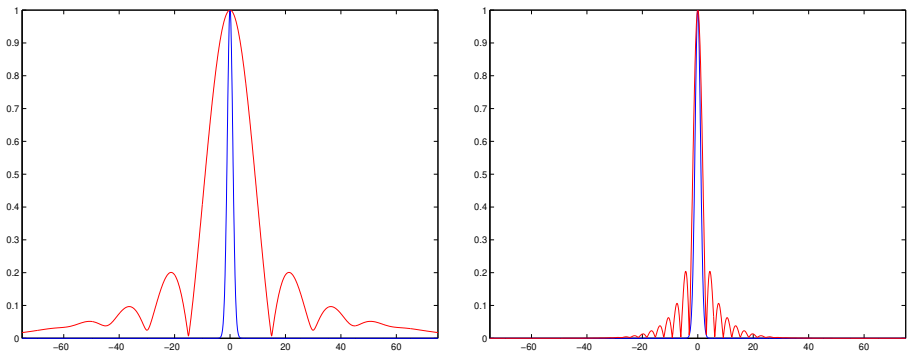

Figure 5: Comparison of the theoretical formula (56) at time $t = 0$, for a medium with $L = 600m$, $a_e = 195m$, $\gamma = 2.12 \times 10^{-5}\, m^{-1}$. THE LEFT FIGURE shows a plot of (56) for a homogeneous medium, $\gamma = 0$, with a TRM of width $a = 40$ (in red / wide Fresnel zone), and the random medium with $\gamma = 2.12 \times 10^{-5}$ and $a = 40$ (in blue / narrow Fresnel zone). THE RIGHT FIGURE shows a plot of (56) for a homogeneous medium, $\gamma = 0$, with $a = a_e = 195$ (in red), and the random medium with $\gamma = 2.12 \times 10^{-5}$, and $a = 40$ (in blue). The match confirms the validity of (57). The values of a_e and γ originate from the numerical estimates of the effective aperture summarized in table 1 in section 8.

8 Numerical Simulations

In this section we present the results of some numerical experiments highlighting the theoretical results of the previous sections. We transmit a time-dependent pulse through the random medium. It is synthesized from 64 frequencies, which allow for enough zero-padding to avoid *aliasing* problems, and at the same time allow for a sufficient number of energy-carrying frequencies to resolve time-domain effects. The unit of length is the peak-energy wavelength, λ_0. We use a discretization with 10 points per wavelength, *i.e.* $\Delta x = \Delta z = 0.1\lambda_0$. For the random medium fluctuations μ we take a Gaussian random field with exponential correlation, constructed spectrally. The correlation length is $\sim 10\lambda_0$, and the maximum contrast is 5%, or 10%.

We use a second order accurate Crank-Nicholson (CN) discretization of the paraxial wave equation

$$2ik\psi_z + \psi_{xx} + k^2\mu\psi = 0, \tag{59}$$

$$\begin{cases} 2ik\delta_z^+\psi_{n,m} & + & \frac{1}{2}\delta_x^+\delta_x^- \left(\psi_{n,m} + \psi_{n+1,m}\right) \\ & + & \frac{1}{2}k^2 \left(\mu_{n+1,m}\psi_{n+1,m} + \mu_{n,m}\psi_{n,m}\right) = 0. \end{cases} \tag{60}$$

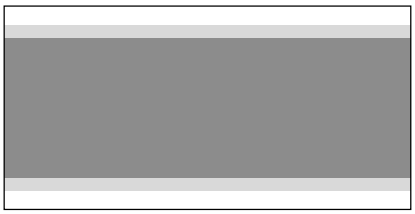

Figure 6: Structure of the numerical domain: In the center strip the random medium is at full strength (75% of the thickness), then there is a smooth transition layer (5–10%) where the strength decreases. In the outer layer the medium is homogeneous, allowing for effective implementation of Discrete Transparent Boundary Conditions.

where

$$(61)\quad \begin{cases} \delta_z^+ \psi_{n,m} &= \frac{\psi_{n+1,m}-\psi_{n,m}}{\Delta z} \\ \delta_x^\pm \psi_{n,m} &= \pm \frac{\psi_{n\pm1,m}-\psi_{n,m}}{\Delta x}. \end{cases}$$

This numerical approach may seem overly direct, for there are widely-used phase-screen methods which do not require sub-wavelength resolution, [DFR85, FRD87]. However, for this series of numerical simulations we really wanted to resolve everything. Our code is limited to 2D. Extension of this direct approach to 3D is no longer viable in the long-range regime that we want to use it. There are, however, good numerical methods for solving the paraxial wave equation in 3D [BCJ98].

We use discrete transparent boundary conditions (DTBCs) to limit the numerical domain while simulating an infinite medium. They are obtained by matching the interior CN-Finite-Difference-Time-Domain (CN-FDTD) scheme with an exact exterior CN-FDTD, yielding an exact *discrete* radiating boundary condition. This is worked out in detail in [Arn95].

We have validated our implementation of the DTBCs for long distances, up to 1000m for random media and up to 5000m for homogeneous media, by comparing the solutions in domains of width $x \in [-w, w]$ to the ones in domains of double the width, $x \in [-2w, 2w]$. In a random medium, or a medium with scatterers, the DTBCs work very well as long as the random medium or the scatterers are sufficiently far away from the boundary. In practice this means about 4–5 λ, with a resolution of 10 points per λ. In this setting, the estimated error is of the order of machine-precision.

In the numerical simulations we use a random medium at full strength in the center 75% of the numerical domain. The strength smoothly approaches zero in a region of 5–10% of the domain-width in order to avoid artificial reflections from the numerical random-homogeneous interface. In the outermost layer of the domain the medium is homogeneous. This allows for effective DTBCs (see figure 6).

The code is written entirely in Matlab, compiled under Matlab 5.2 with compiler 1.2 and Matlab 5.3 with compiler 1.2.1. A typical simulation, with a 1000m $\times$ 200m numerical domain, and 64 frequencies, completes in approximately 22 hours, on a dual-Pentium-III Xeon 550MHz Linux workstation, where the embarrassingly parallel nature of the problem is exploited.

8.1 Numerical Results

We show numerical results for propagation through random media with maximum fluctuations contrast of 10%, *i.e.* $|\mu| \leq 0.1$. This is actually quite a lot of randomness and is really pushing the validity of the paraxial approximation. The reason we use such high contrast is to observe super-resolution phenomena in a numerical domain that is manageable on a small network of workstations.

The width of the finite-aperture TRM is 50m, and the numerical domain in 200m wide. Simulations for three different propagation distances are shown. *(i)* When the propagation distance is short, only 200 meters. As can be seen in figure 7, this distance is too short for the randomness to have an impact on the resolution of the self-averaging, time-reversed and back-propagated signal. *(ii)* With a propagation distance of 600 meters the super-resolution effect is quite noticeable. The peak of the re-compressed signal in the random medium is about 40% higher and quite a bit narrower than the one in the homogeneous medium. This is very stable from realization to realization and figure 8 shows a typical case. *(iii)* As we increase the propagation distance to 1000 meters, more energy spills out of the domain by radiation through the boundaries, and multipathing contributing to super-resolution is lost. In figure 9 we are past the limit of what our numerical setup can do.

8.2 Numerical limits

For a given width of the numerical domain, and of the random medium, there is a limit to how long a propagation distance can be used in the numerical experiments. As the effective aperture, a_e exceeds the size of the domain, the configuration can no longer accurately model an infinite medium. In table 1 we show estimates for a_e and for the medium-characterizing parameter γ, in inverse meters, for different propagation distances with fixed domain and TRM-widths.

It is reasonable to expect the growth of $a_e(L)$ with L for the finite aperture case to be similar to the one for a Gaussian aperture, that is, $\sim \sqrt{\gamma L^3}$ as in equation (53). We have found from the numerical simulations that a_e, a, and γ are related by equation (57), for a finite aperture TRM. If we use this formula to estimate γ, we might expect it to approach a constant as we sample an increasing part of the random medium. However, table 1 and figure 10 show that this is not the case. Given the width of the numerical domain, there is a range of propagation distances for which the estimated γ is close to constant. For larger propagation distances there is a drop-off since the numerical setup cannot adequately capture the multipathing and the growing effective aperture. The numerical limitations of the effective aperture formula (57) are more severe

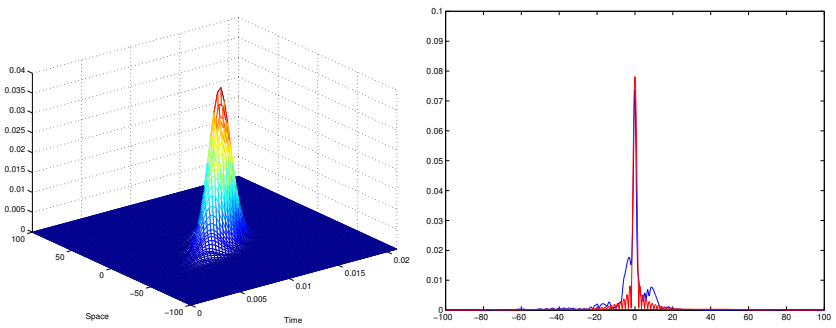

(a) TRM-received (b) Recompressed

Figure 7: Numerical simulation of time-reversal. The width of the time reversal mirror and the numerical domain are 50m, and 200m, respectively. The maximum contrast is $\pm 10\%$, that is $|\mu| \leq 0.1$. The left figure shows the signal as received on the TRM-plane. This signal is restricted to the mirror, time-reversed, and re-emitted into the medium. The right figure shows a spatial section through the re-focussed signal. Here, the propagation distance is very short, only 200m, or about 20 correlation lengths. We see that there is not enough randomness to observe super-resolution.

in our setup than the theoretical ones coming from the beam approximation and discussed at the end of section 7.

Our numerical calculations show that it is hard to simulate super-resolution with long propagation distances. We have used more than 200 time-harmonic realizations per propagation distance to estimate γ and a_e, whereas the self-averaging for figures 7–9 uses only 64 frequencies, and one realization of the random medium, and cannot therefore be expected to be as stable statistically. By using more frequencies, and widening the medium, these simulations should become more stable statistically.

9 Dynamic TRM Placement

It is possible that the main part of the energy misses a statically placed time reversal mirror. This can occur when the medium has a systematic drift (cross-wind), or when the randomness is anisotropic. In such cases it may be advantageous to be able to move the TRM laterally so as to capture as much energy as possible. In this section we consider the effects of dynamic placement of the TRM. At this time, we do not have a theory that covers dynamic TRM placement, so the study is numerical.

We dynamically move the TRM with infinite speed, that is, we place the TRM in the optimal lateral location where it captures the most energy.

We show two realizations, each for the time-reversal experiment for a propa-

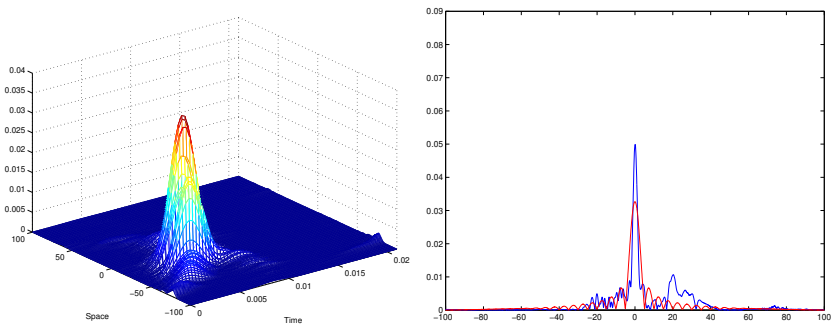

(a) TRM-received (b) Recompressed

Figure 8: In this simulation the propagation distance is 600m. Now we clearly see the super-resolution phenomenon: the peak of the re-compressed pulse in the random medium (blue) is sharper than the one for the homogeneous medium (red). (All other parameters are as in figure 7.)

gation distance of 600 meters (figure 11) and 1000 meters (figure 12), comparing the centered static placement with the dynamic placement. For the first realization in figure 11, the pulse energy is quite smeared out when it reaches the TRM plane, and the statically placed screen just barely manages to capture enough information to resolve the source. The dynamically placed TRM re-compression is approximately 3 times better, and clearly super-resolves the source. In the second realization in figure 11, the pulse energy is still quite concentrated when it reaches the TRM-plane, but it is a little bit off-center, so moving the mirror enhances the re-compression.

As discussed earlier, in section 8.2, the 1000-meter propagation calculation cannot capture enough multipathing to give an accurate picture of super-resolution. However, as can be seen in the first realization shown in figure 12, dynamic placement can improve the re-compression, even in this case. There are settings, as in the second realization, when the energy is too spread out, where dynamic placement does not help.

10 Time Reversal in a Wave Guide

In this section we briefly explore numerically time-reversal in random media where the boundaries are strongly *reflecting*, so that the energy gets trapped as in a *wave-guide*. This is physically the case in underwater acoustics, where sound is reflected from the surface and from the bottom of the ocean, or in sound propagation in a channel.

Dirichlet or Neumann boundary conditions are, of course, a very simplified way to account for the physical boundaries where the surface is rippled, and the bottom rough. However, it is still of interest to see how the reflections off the

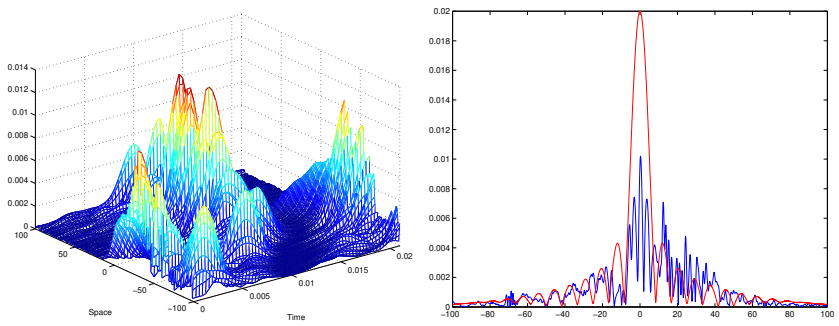

(a) TRM-received (b) Recompressed

Figure 9: In this simulation the propagation distance is 1000m. Although the first peak of the recompressed signal in the random medium is much narrower, there is really no super-resolution in this case because of the large side-lobes. The limits of the numerical simulations are discussed in section 8.2. (All other parameters as in figure 7.)

boundaries and the randomness of the medium interact. We use homogeneous Dirichlet boundary conditions in our numerical simulations.

We compare time reversal through homogeneous and random media in a series of numerical calculations as follows. The numerical domain has width 100m, the propagation distance is 800m and the maximum contrast, in the random case, is 10%. The first, and third numerical experiments, (figure 13 and figure 15), are standard time-reversal in an infinite domain (radiating boundary conditions), with a statically placed TRM. The second and fourth experiments are in a wave-guide with zero (Dirichlet) boundary conditions. In the second case (figure 14), the TRM is of the same width as the domain, so it captures all available energy and the re-compressed signals are very good for both the homogeneous and random media. In the forth, and most interesting case (figure 16), the TRM is 60m (or 60% of the wave-guide), and we clearly see how the randomness help us achieve super-resolution. The side-lobes are are eliminated by multipathing inside the wave-guide.

We also consider smaller TRMs, in the same setting, to make sure that the results for 60 meters (figure 16 are not special or nontypical. In figure 17, where the TRM width is 50m, we see clearly that the incoherence induced by the randomness dampens the side-lobes and the peak is much better resolved in the random case. This is super-resolution in a wave-guide.

11 Summary and Conclusions

We have presented a detailed analytical and numerical study of how multipathing in random media enhances resolution in time-reversed acoustics, that is, how super-resolution arises in random media. We have clarified, in particu-

$\mathbf{L}$	$\mathbf{a_e^E}$	γ	$\mathbf{a_e^T}$	$\mathbf{N}$
300	77	2.00×10^{-5}	77	207
350	86	1.69×10^{-5}	92	418
400	104	1.83×10^{-5}	109	202
450	123	1.86×10^{-5}	127	202
500	150	2.11×10^{-5}	147	205
600	195	2.12×10^{-5}	190	213
650	217	2.08×10^{-5}	213	260
700	248	2.19×10^{-5}	238	202
750	266	2.05×10^{-5}	263	235
800	275	1.81×10^{-5}	289	201
850	293	1.71×10^{-5}	316	223

Table 1: The table shows the propagation distance, L in meters; the numerically estimated effective aperture, a_e^E in meters; the corresponding estimate for γ, in inverse meters, using equation (57); a "theoretical" effective aperture, a_e^T computed using (57) with $\gamma = 2.12 \times 10^{-5}$ (the median of the estimated γs); and the number of realizations used for each estimated pair of (a_e^E, γ). The other parameters are: TRM width, $a = 40m$; maximal contrast 10%, width of the numerical domain 150m; width of the random media 112.5m.

lar, the statistical stabilization of the re-compressed pulse in the time domain. We have also shown that when the propagation distance is large compared to the wavelength and the correlation length of the inhomogeneities, and the Time Reversal Mirror is small, then there is an exact expression for the effective size of the TRM, its *effective aperture* (57), valid in both in the time and frequency domain. Multipathing makes the effective size of the TRM much larger than its physical size. We have verified the theoretical results with careful and extensive numerical calculations, using exact non-reflecting boundary conditions in one transverse direction to simulate an infinite medium. Full two dimensional transverse propagation is intractable on a workstation, at present, especially for long distances. This is because the discrete transparent boundary conditions are non-local.

A Comments and References for the Transport Approximation

The paraxial equation (2), or (4), is a Schrödinger equation in which z plays the role of time and the fluctuations $\mu = n^2 - 1$ are the random, "time" dependent potential. When these fluctuations are δ-correlated in z then we have exact

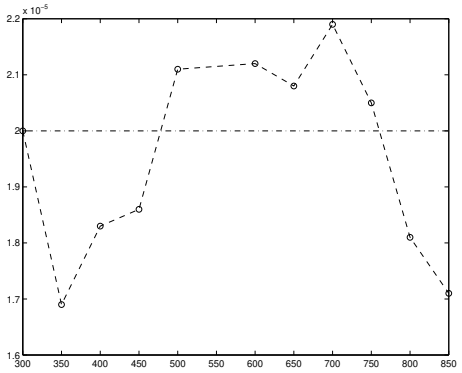

Figure 10: The estimated values of γ for table 1. The estimate stabilizes as the propagation distance increases, *until* the numerical setup cannot capture adequately the multipathing and the rapidly growing effective aperture. In our setup we can simulate an effective aperture up to about twice the width of the random medium.

closed equations for moments of products of Green's functions

$$(62)\quad \left\langle \prod_{j=1}^{N} G(L,0,\mathbf{x}_j,\xi;k_j) \prod_{j=N+1}^{N+M} \overline{G(L,0,\mathbf{x}_j,\xi;k_j)} \right\rangle,$$

where ξ is the source location, $\mathbf{x}_j$ are observation points and the wave numbers k_j may be the same or different. This is done in [Fur93] or in the articles in [TIZ93], and in a more mathematical way in [DP84]. In the case of two factors, $N = M = 1$, the product is denoted by Γ, and satisfies (9). The mean of its Fourier transform (13) is the mean Wigner function that now satisfies equation (38) *exactly*. The power spectral density $\widehat{R}$ is a function of $\mathbf{P} - \mathbf{Q}$ only, so the transport equation (38) is a convolution equation and can be solved explicitly. One can then do the narrow beam approximation as we did in section 7, and this can be found in the literature in many places, in [Fur93] as well as in this appendix. The white noise or δ-correlation limit leading to (38) is also considered in [BP84].

The mathematical idealization of having δ correlated fluctuations is relevant in many situations in underwater acoustics and in many other propagation problems, as we will explain in this appendix with a careful scaling of the problem. Using δ correlated fluctuations is convenient analytically but may obscure other limits that are relevant, such as the high frequency limit. This makes little difference for *single* frequency statistics but it needs to be analyzed carefully in order to explain pulse stabilization in the time domain, as discussed in section 6. That is why we presented the resolution analysis of time reversal in a random medium as we did here.

When backscattering is important then the transport approximation is more involved and must be used carefully. A theory for the transport approximation

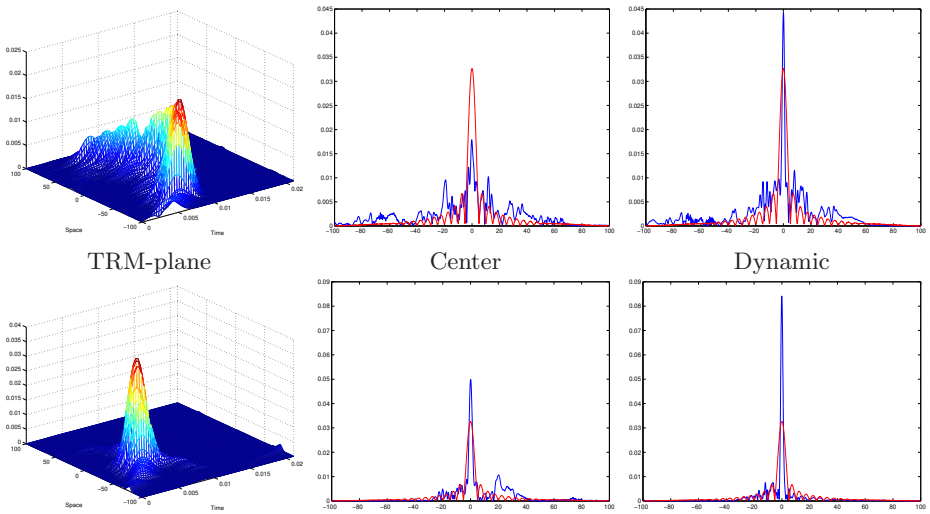

Figure 11: Dynamic TRM placement: 600m propagation. The Left Figure shows the pulse in space-time as received on the TRM-plane. The Center Figure shows a spatial cut through the peak of the re-compressed pulse using static TRM placement. The Right Figure shows a spatial cut through the peak of the re-compressed pulse using optimal dynamic TRM placement. Note that each plot is for one random realization of the medium. The maximum contrast is 10%, that is $|\mu| \leq 0.1$. The TRM is 50 meters wide and the numerical domain 200 meters wide. The red curves correspond to time-reversal in a homogeneous medium and the blue curves to time-reversal in the random medium.

using Wigner functions is given in [RPK96] where many other references can be found. A recent survey of transport theory for random media is [vRN99]. Time reversal in randomly *layered* media is analyzed in [CF97]. Transport theory in a waveguide is considered in [KP77].

A.1 Scaling I

We will now consider some specific scalings that result in the phase diffusion equation (47), *and* have the frequency decorrelation property (41) that gives pulse stabilization.

We begin by rewriting the Schrödinger equation (2) or (4) in dimensionless form. Let L_z and $L_{\mathbf{x}}$ be characteristic length scales in the propagation direction, the distance L between the source and the TRM for example, and in the transverse direction, respectively, and k_0 a characteristic wave number. We introduce a dimensionless wave number $k' = k/k_0$ with $k_0 = \omega_0/c_0$ and ω_0 a central frequency. We rescale $\mathbf{x}$ and z by $\mathbf{x} = L_{\mathbf{x}}\mathbf{x}'$, $z = L_z z'$ and rewrite (2) in

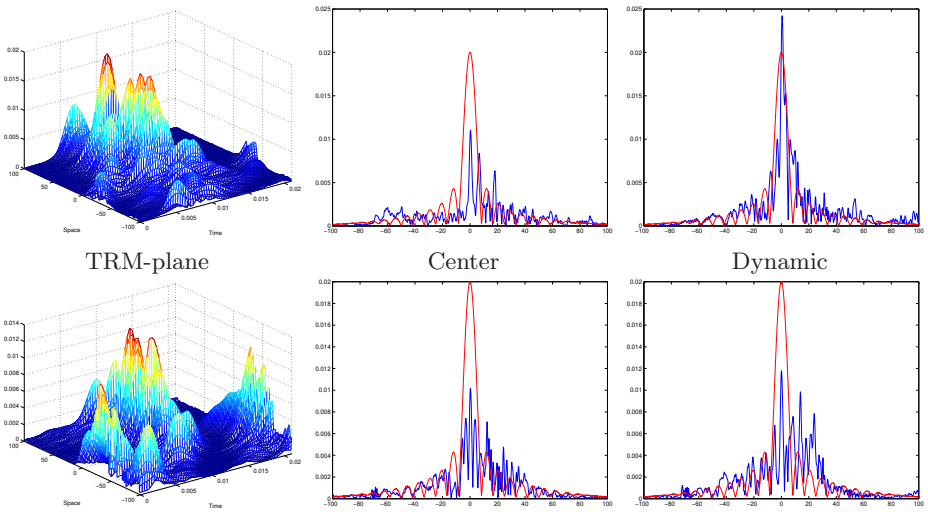

Figure 12: Dynamic TRM placement: `1000m` propagation. (For parameter information see the caption for figure 11).

the new coordinates dropping the primes:

$$2ik\frac{\partial\psi}{\partial z}+\frac{L_z}{k_0L_{\mathbf{x}}^2}\Delta\psi+k^2k_0L_z\sigma\mu\left(\frac{\mathbf{x}L_{\mathbf{x}}}{l},\frac{zL_z}{l}\right)\psi=0. \tag{63}$$

The physical parameters that characterize the propagation problem are: (a) the central wave number k_0, (b) the strength of the fluctuations σ, and (c) the correlation length l. The length scales $L_x,\ L_z$ and the central wave length $\lambda_0=2\pi/k_0$ characterize the propagation regime that we wish to consider. The random fluctuations μ are normalized to have unit variance and unit correlation length. We introduce now three dimensionless variables

$$\delta=\frac{l}{L_{\mathbf{x}}},\quad \epsilon=\frac{l}{L_{\mathbf{z}}},\quad \beta=\frac{1}{k_0l} \tag{64}$$

which are, respectively, the reciprocals of the *transverse scale* relative to correlation, the *propagation distance* relative to correlation, and the correlation length relative to the central *wave length*. We will assume first that the dimensionless parameters β, σ and δ are small

$$\beta\ll 1,\quad \sigma\ll 1,\quad \delta\ll 1\ . \tag{65}$$

This is a regime of parameters where super-resolution phenomena as described here can be observed. It is a high-frequency regime ($\lambda\ll l,\ \beta\ll 1$), not the one on which the paper is based, but it is important physically and is easier to deal with analytically. The 'transport' regime ($\beta\sim 1$) that we analyze in the paper is taken up after, as is the regime $\epsilon\ll 1$ that gives white noise.

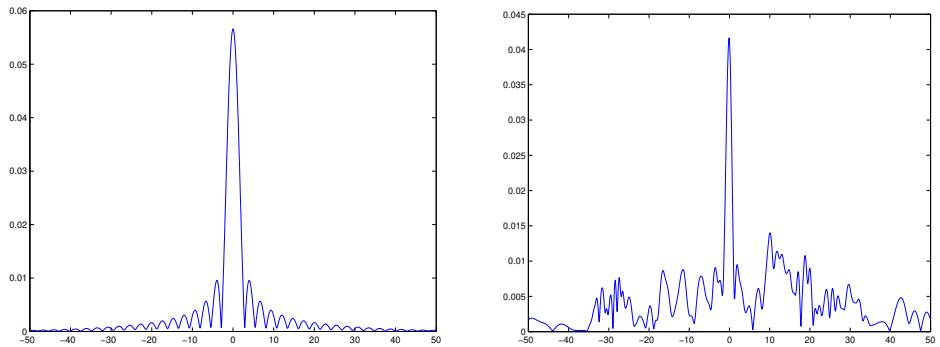

Figure 13: The re-compressed pulse for homogeneous (left) and random (right) media. The propagation distance is 800m, the domain width is 100m, and the maximal contrast is 10%. The boundary conditions are: *DTBC*. TRM width *100m*. Here, we can see clearly super-resolution as the re-compressed peak is narrower in the random medium.

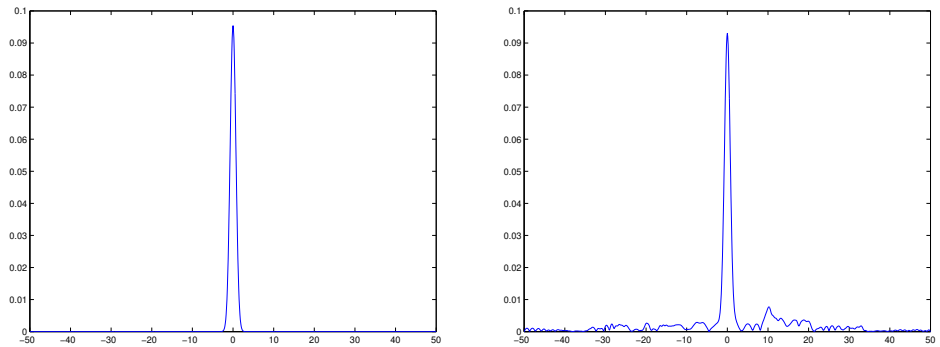

Figure 14: Homogeneous medium on the left, random medium on the right. Here we have *Wave-Guide* boundary conditions with TRM width *100m*. We capture all the energy inside the wave-guide on the TRM, so the wave-guide effect is much stronger than the random-medium effect. There can be no super-resolution in this setting.

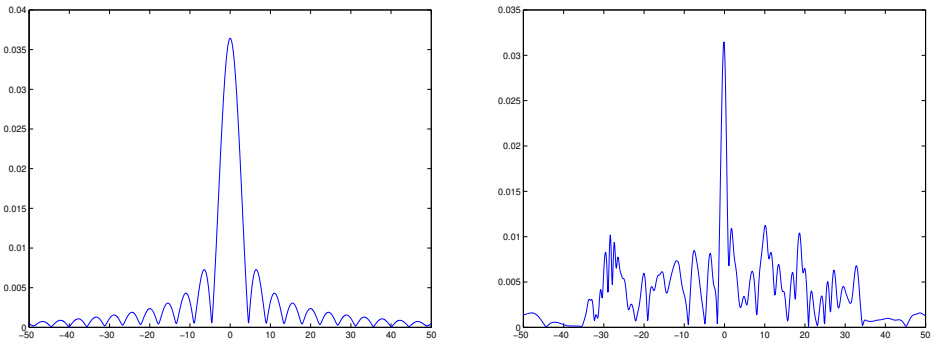

Figure 15: Homogeneous medium on the left, random medium on the right. Type of boundary conditions: *DTBC* with TRM width *60m*. We can clearly see super-resolution as the re-compressed peak is narrower in the random medium case. The fluctuations in the side-lobes are partly due to the fact that we are pushing the paraxial approximation beyond its limit; the 10% contrast is stretching the "low-contrast" assumption.

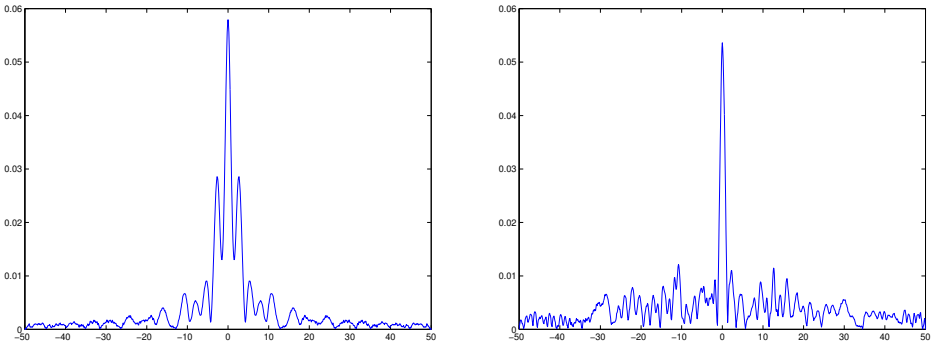

Figure 16: Homogeneous medium on the left, random medium on the right. Type of boundary conditions: *Wave-Guide* with TRM width *60m*. The wave-guide effects are quite strong, but an argument for super-resolution can be made, since the peak is better defined. Randomness does not, in any case, degrade the results.

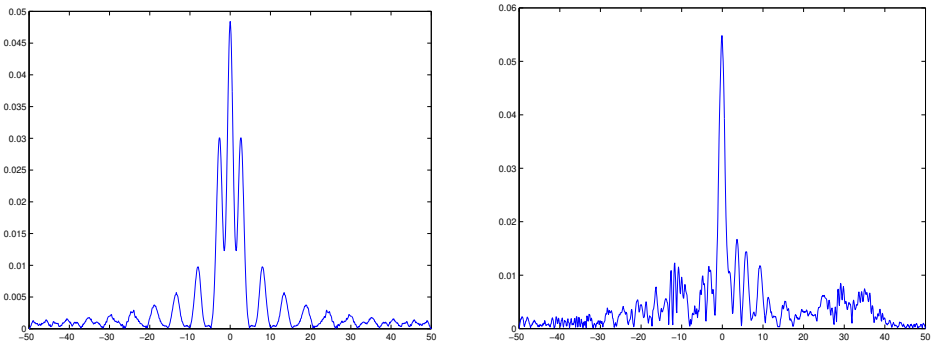

Figure 17: Homogeneous medium on the left, random medium on the right. Type of boundary conditions: *Wave-Guide* with TRM width *50m*. The wave-guide effects are quite strong, but there is super-resolution since the peak is better defined in the random medium.

The Fresnel number is defined by

$$\theta = \frac{L_z}{k_0 L_{\mathbf{x}}^2} = \beta \frac{\delta^2}{\epsilon} \tag{66}$$

After multiplying by θ we can rewrite the Schrödinger equation (63) in the form

$$2ik\theta\psi_z + \theta^2 \Delta_{\mathbf{x}}\psi + \frac{k^2}{\epsilon^{1/2}}\mu(\frac{\mathbf{x}}{\delta}, \frac{z}{\epsilon})\psi = 0. \tag{67}$$

provided that we relate ϵ to σ and δ by

$$\epsilon = \sigma^{2/3}\delta^{4/3}. \tag{68}$$

The asymptotic regime (65) is realized with the ordering

$$\theta \ll \epsilon \ll \delta \ll 1\ , \tag{69}$$

which implies that $\beta \ll 1$ also holds, corresponding to the *high-frequency limit*. We see from the scaled Schrödinger equation (67) that this regime has the following interpretation. We have first take a *high frequency* limit $\theta \to 0$, then a *white noise* limit $\epsilon \to 0$, and then a *broad beam* limit $\delta \to 0$. We will now discuss briefly and interpret these limits. A full analysis is given in [PRS01]. Other orderings are considered in the next section.

For the high frequency limit, especially in random media, we use the Wigner function as we explained before. Let $\psi_\theta(z, \mathbf{x})$ be a solution of the rescaled Schrödinger equation (67). The Wigner function depends on the propagation distance z, the transverse position $\mathbf{x}$ and wave vector $\mathbf{p}$, and is given by

$$W_\theta(z, \mathbf{X}, \mathbf{P}) = \int_{\mathbb{R}^d} \frac{d\mathbf{y}}{(2\pi)^d} e^{i\mathbf{P}\cdot\mathbf{Y}} \psi_\theta(z, \mathbf{X} - \frac{\theta\mathbf{Y}}{2}) \overline{\psi_\theta(z, \mathbf{X} + \frac{\theta\mathbf{Y}}{2})}. \tag{70}$$

It satisfies the evolution equation

$$\frac{\partial W_\theta}{\partial z} + \frac{\mathbf{P}}{k}\cdot\nabla_{\mathbf{X}} W_\theta = \frac{ik}{2\sqrt{\epsilon}}\int e^{i\mathbf{Q}\cdot\mathbf{X}/\delta}\widehat{\mu}\left(\mathbf{Q},\frac{z}{\epsilon}\right)\frac{W_\theta\left(\mathbf{P}-\frac{\theta\mathbf{Q}}{2}\right)-W_\theta\left(\mathbf{P}+\frac{\theta\mathbf{Q}}{2}\right)}{\theta}\frac{d\mathbf{Q}}{(2\pi)^d}.$$

In the limit $\theta\to 0$ the solution converges in a suitable weak sense, for each realization, to the solution of the random Liouville equation

$$\frac{\partial W}{\partial z} + \frac{\mathbf{P}}{k}\cdot\nabla_{\mathbf{X}} W + \frac{k}{2\sqrt{\epsilon}}\nabla_{\mathbf{X}}\mu\left(\frac{\mathbf{x}}{\delta},\frac{z}{\epsilon}\right)\cdot\nabla_{\mathbf{P}} W = 0. \tag{71}$$

The initial condition at $z=0$ is that W equals to the limit Wigner function $W_0(\mathbf{X},\mathbf{P})$ of the initial wave function. This is, of course, what we expect in the high frequency limit since the characteristics of (71) are the ray equations in the random medium.

We next consider the white noise limit $\epsilon\to 0$ in the random Liouville equation (71). Then $W_\epsilon(z,\mathbf{X},\mathbf{P})$ converges weakly (in a probabilistic sense) to the stochastic process $W(z,\mathbf{X},\mathbf{P})$ that satisfies the Itô stochastic partial differential equation

$$dW = \left[-\frac{\mathbf{P}}{k}\cdot\nabla_{\mathbf{X}} W + \frac{k^2 D}{2}\Delta_{\mathbf{P}} W\right]dz - \frac{k}{2}\nabla_{\mathbf{P}} W\cdot d\mathbf{B}(\frac{\mathbf{X}}{\delta},z). \tag{72}$$

Here $\mathbf{B}(\mathbf{X},z)$ is a Brownian random field, that is, a Gaussian process with mean zero and covariance

$$\langle\, B_i(\mathbf{X}_1,z_1)B_j(\mathbf{X}_2,z_2)\,\rangle = -\left(\frac{\partial^2 R_0((\mathbf{X}_1-\mathbf{X}_2))}{\partial X_i\partial X_j}\right)\min\{z_1,z_2\}.$$

where

$$R_0(\mathbf{X}) = \int_{-\infty}^{\infty} R(s,\mathbf{X})ds\ , \quad R(z,\mathbf{X}) = \langle\,\mu(s+z,\mathbf{Y}+\mathbf{X})\mu(s,\mathbf{Y})\,\rangle\,,$$

and

$$D = -\frac{1}{16}\Delta R_0(0),$$

which is the negative Laplacian of the reduced covariance R_0 at zero. We call equation (72) the Itô-Liouville equation. Note that the Brownian field that enters the stochastic partial differential equation (72) depends explicitly on the dimensionless correlation length δ in the transverse direction. Therefore the limit process also depends on δ. Note also that the average of W, $\langle\, W(z,\mathbf{X},\mathbf{P})\,\rangle$, satisfies the phase space diffusion equation (47) but with a diffusion constant D that differs from (48). The first argument of $\widehat{R}$ in the integral in (48) is now set to zero, which then becomes the Fourier transform of the reduced covariance R_0. The D above agrees with (48) after this change. A detailed discussion of

the white noise limit is in [PRS01] and the theoretical background of stochastic partial differential equations like (72) is presented in [Kun97].

From the Itô-Liouville equation (72) we can get closed equations for all the moments of the Wigner function W, not only for its mean, as well as for moments with different wave numbers k. The wave number enters (72) as a parameter. To have the decorrelation property (41) we need to show that

$$(73)\quad \langle\, W(z,\mathbf{X},\mathbf{P};k_1)W(z,\mathbf{X},\mathbf{P};k_2)\,\rangle \approx \langle\, W(z,\mathbf{X},\mathbf{P};k_1)\,\rangle\,\langle\, W(z,\mathbf{X},\mathbf{P};k_2)\,\rangle$$

for $k_1 \neq k_2$. This is true in the limit $\delta \to 0$, as is explained in detail in [PRS01], because it is as if the Brownian fields $\mathbf{B}$ in (72) have spatial correlation zero. After a scaling change this translates into decorrelation for different wave numbers.

We can summarize the results of doing the scaling limits $\theta \to 0$, followed by $\epsilon \to 0$, followed by $\delta \to 0$ by noting that they represent a precise analytical way to study the regime where the wavelength is much smaller than the correlation length (high frequency limit), the propagation distance is much larger than the correlation length and the fluctuations are weak (white noise limit), and the transverse length scale is much larger than the correlation length ($\delta \to 0$). The first two limits are fully compatible with the paraxial or parabolic wave approximation of Section 2, while the last one requires that the beam, which is narrow because of the first two limits, must not be too narrow. Note that this scalimg limit analysis is different from the one we use in the paper, but appropriate for underwater acoustics. It leads to the same phase space diffusion equation (47) for $\langle\, W(z,\mathbf{x},\mathbf{p})\,\rangle$ but the structure of the higher moments is different here, coming from (72), than under the scaling followed in the paper. We now consider this scaling.

A.2 Scaling II

The second scaling we want to consider is the one described in Section 5, where the wavelength is comparable to the correlation length, $\lambda \sim l$, the small parameter $\epsilon = \frac{\lambda}{L_z} \ll 1$ and the standard deviation of the fluctuations $\sigma \sim \sqrt{\epsilon}$. The scaled Schrödinger equation follows from (33) and has the form

$$2ik\epsilon\psi_z + \epsilon^2\Delta_{\mathbf{x}}\psi + k^2\epsilon^{1/2}\mu(\frac{\mathbf{x}}{\epsilon},\frac{z}{\epsilon})\psi = 0.$$

To connect with the precise scaling of (67) we simply have to set $\theta = \epsilon$, $\delta = \epsilon$ and $\epsilon = \sigma^2$, which implies that $\beta = 1$. This is the transport scaling. If however we want to follow this with the narrow beam limit of Section 7 we must allow for different horizontal and vertical length scales by letting

$$(74)\quad \zeta = \frac{\epsilon}{\delta},$$

which from (66) gives

$$\zeta^2\theta = \epsilon\beta.$$

With $\sigma = \zeta\sqrt{\epsilon}$, the scaled Schrödinger equation now is

$$2ik\zeta^2\epsilon\beta\psi_z + (\epsilon\beta)^2\Delta_{\mathbf{x}}\psi + k^2\zeta^3\sqrt{\epsilon}\mu(\frac{\zeta\mathbf{x}}{\epsilon}, \frac{z}{\epsilon})\psi = 0.$$

Letting $\epsilon \to 0$ with β and ζ fixed is the *transport limit*. Letting $\beta/\zeta \to 0$ is the high frequency, phase space diffusion limit and letting $\zeta \to 0$ restores the validitiy of the parabolic approximation. We refer to these last two limits as the *narrow beam approximation*.

The transport limit is analyzed in [RPK96] and in [BPR01], where a rigorous proof of convergence of the mean Wigner function is given. It is the same as (38) in Section 5 except that we now have the parameters β and ζ so that the average Wigner function satisfies

$$(75)\begin{cases} k\frac{\partial W}{\partial L} + \mathbf{P}\cdot\nabla_{\mathbf{X}}W = \frac{\pi k^3\zeta^4}{4\beta^4}\cdot \\ \quad \int \widehat{R}\left(\frac{\zeta^2(\mathbf{P}^2-\mathbf{Q}^2)}{2k\beta}, \frac{\zeta(\mathbf{P}-\mathbf{Q})}{\beta}\right)\Big[W(L,\mathbf{X},\mathbf{Q};\xi,\eta;k) - W(L,\mathbf{X},\mathbf{P};\xi,\eta;k)\Big]\, d\mathbf{Q} \end{cases}$$

The narrow beam limit $\beta/\zeta \to 0$ followed by $\zeta \to 0$ comes from a two term Taylor expansion of the integrand in (75), leading to the phase space diffusion equation (47) with the phase space diffusion coefficient given by

$$D(\mathbf{P}) = \int \widehat{R}\left(\zeta\tfrac{\mathbf{P}\cdot\mathbf{Q}}{k}, \mathbf{Q}\right)|\mathbf{Q}|^2\, d\mathbf{Q}.$$

We must now let $\zeta \to 0$ as well, otherwise the parabolic approximation itself may be violated. This will then give the same phase diffusion coefficient obtained in the high frequency limit (69) of the previous section.

What we have not been able to show in [BPR01] is that in the transport limit the decorrelation property (73) holds exactly. However, formal asymptotic analysis as well as numerical simulations indicate that this is true even though a mathematical proof is lacking at present.

Let us make some remarks that contrast the scaling limits of this and the previous section. The frequency decorrelation property is a consequence of the transport limit $\epsilon \to 0$ and does not depend on the narrow beam limit $\beta/\zeta \to 0$ and $\zeta \to 0$. The narrow beam limit gives not only an important analytical simplification leading to an easy to solve phase space diffusion equation. It is in a way an essential part of the theory because without it the paraxial approximation is unlikely to hold in the transport limit. The validity of the paraxial approximation is, however, re-established after the narrow beam approximation. Note also that $\zeta \to 0$ brings in the anisotropy between horizontal and transverse length scales that is needed in the paraxial approximation.

The *white noise limit* corresponds to the ordering

$$(76)\quad \epsilon \ll \theta \ll \delta \ll 1,$$

with $\sigma = \delta^{-2}\epsilon^{3/2}$. It is different from both the *transport limit* of this section

$$(77)\quad \epsilon \ll \beta \ll \zeta \ll 1,$$

as well as the *high frequency limit*

(78) $\theta \ll \epsilon \ll \delta \ll 1,$

(69) of the previous section. However, our analysis [PRS01] shows that in all cases the average Wigner function satisfies the same phase space diffusion equation (47). We expect that the structure of the higher order moments, including the frequency decorrelation property, will also be the same but we can only show this in the high frequency limit (69) and the white noise limit (76), where the Itô-Liouville equation (72) characterizes the Wigner function fully. The fact that several different asymptotic scale orderings lead to the same limit behavior explains why super-resolution and statistical stability in time reversal are seen very clearly both in physical experiments and in numerical simulations.

We also expect that the full wave transport limit [RPK96], without the paraxial approximation, will have the frequency decorrelation property and hence pulse stabilization. This has been seen clearly in full wave numerical simulations in random media [TP01, BBPT01].

References

[AKP+91] M. Asch, W. Kohler, G. Papanicolaou, M. Postel, and B. White. Frequency Content of Randomly Scattered Signals. *SIAM Review*, 33:519–626, 1991.

[Arn95] Anton Arnold. Numerically Absorbing Boundary Conditions for Quantum Evolution Equations. In *Proceedings of the International Workshop on Computational Electronics*, Tempe, USA, 1995.

[BBPT01] J. Barryman, L. Borcea, G. Papanicolaou, and C. Tsogka. Imaging and time reversal in random media. *Journal of the Acoustical Society of America*, submitted, 2001.

[BCJ98] Eliane Bécache, Francis Collino, and Patrick Joly. Higher-order Numerical Schemes and Operator Splitting for Solving 3D Paraxial Wave Equations in Heterogeneous Media. Technical Report 3497, INRIA: Institute National de Recherche en Informatique et en Automatique, September 1998.

[BEHJ88] A. Bamberger, B. Engquist, L. Halpern, and P. Joly. Parabolic Wave Equation Approximations in Heterogeneous Media. *SIAM Journal on Applied Mathematics*, 48(1):99–128, February 1988.

[BP84] R. Bouc and E. Pardoux. Asymptotic analysis of PDEs with wide-band noise disturbances and expansion of the moments. *Stochastic Analysis and Applications*, 2:369–422, 1984.

[BPR01] Guillaume Bal, George Papanicolaou, and Leonid Ryzhik. Radiative transport in a time dependent random medium. *Journal of Statistical Physics*, submitted, 2001.

[CF97] J. F. Clouet and J. P. Fouque. A time-reversal method for an acoustical pulse propagating in randomly layered media. *Wave Motion*, 25:361–368, 1997.

[DFR85] Roger Dashen, Stanley M. Flatté, and Stephen A. Reynolds. Path-integral Treatment of Acoustic Mutual Coherence Functions for Rays in a Sound Channel. *Journal of the Acoustical Society of America*, 77(5):1716–1722, May 1985.

[DJ90] David R. Dowling and Darrell R. Jackson. Phase Conjugation in Underwater Acoustics. *Journal of the Acoustical Society of America*, 89:171–181, January 1990.

[DJ92] David R. Dowling and Darrell R. Jackson. Narrow-band Performance of Phase-conjugate Arrays in Dynamic Random Media. *Journal of the Acoustical Society of America*, 91:3257–3277, June 1992.

[DP84] D. A. Dawson and G. Papanicolaou. A Random Wave Process. *Applied Mathematics and Optimization*, 12:97–114, 1984.

[DRF95] Arnaud Derode, Philippe Roux, and Mathias Fink. Robust Acoustic Time Reversal with High-Order Multiple Scattering. *Physical Review Letters*, 75(23):4206–4209, December 1995.

[Fin97] Mathias Fink. Time Reversed Acoustics. *Physics Today*, pages 34–40, March 1997.

[Fin99] Mathias Fink. Time-Reversed Acoustics. *Scientific American*, pages 91–97, November 1999.

[FRD87] Stanley M. Flatté, Stephen A. Reynolds, and Roger Dashen. Path-integral Treatment of Intensity Behaviour for Rays in a Sound Channel. *Journal of the Acoustical Society of America*, 82(3):967–972, September 1987.

[Fur93] K. Furutsu. *Random Media and Boundaries: Unified Theory, Two-Scale Method, and Applications*. Springer Verlag, 1993.

[HSK+99] W. S. Hodgkiss, H. C. Song, W. A. Kuperman, T. Akal, C. Ferla, and D. R. Jackson. A Long-Range and Variable Focus Phase-Conjugation Experiment in Shallow Water. *Journal of the Acoustical Society of America*, 105(3):1597–1604, March 1999.

[KHS+97] W. A. Kuperman, W. Hodgkiss, H. C. Song, T. Akal, C. Ferla, and D. R. Jackson. Phase Conjugation in the Ocean. *Journal of the Acoustical Society of America*, 102(6):1–16, December 1997.

[KP77] Werner Kohler and George Papanicolaou. *Wave propagation in a randomly inhomogeneous ocean*. Lecture Notes in Physics 70, Wave Propagation and Underwater Acoustics. Springer-Verlag, 1977.

[Kun97] H. Kunita. *Stochastic flows and stochastic differential equations*. Cambridge University Press, 1997.

[Por89] R. P. Porter. *Generalized Holography with Application to Inverse Scattering and Inverse Source Problems*. Number XXVII in Progress in Optics. Elsevier Science Publishers, 1989.

[PRS01] George Papanicolaou, Leonid Ryzhik, and Knut Solna. The parabolic approximation and time reversal in a random medium. *SIAM Journal on Applied Mathematics*, submitted, 2001.

[RPK96] L. V. Ryzhik, G. C. Papanicolaou, and J. B. Keller. Transport Equations for Elastic and Other Waves in Random Media. *Wave Motion*, 24:327–370, 1996.

[SP00] Knut Solna and George Papanicolaou. Ray Theory for a Locally Layered Random Medium. *Random Media*, 10:155–202, 2000.

[Tap77] F. D. Tappert. *The Parabolic Approximation Method*. Lecture Notes in Physics 70, Wave Propagation and Underwater Acoustics. Springer Verlag, 1977.

[TIZ93] V. I. Tatarskii, A. Ishimaru, and V. U. Zavorotny, editors. *Wave Propagation in Random Media (Scintillation)*. SPIE and IOP, 1993.

[TP01] C. Tsogka and G. Papanicolaou. Time reversal through a solid-liquid interface and super-resolution. *Journal of the Acoustical Society of America*, submitted, 2001.

[vRN99] M. C. W. van Rossum and Th. M. Nieuwenhuizen. Mutiple Scattering of Classical Waves: Microscopy, Mesoscopy, and Diffusion. *Reviews of Modern Physics*, 71(1):313–371, January 1999.